

Effect of Different Infill Types and Welding Separation on the Cyclic Behavior of Steel Shear Walls

Osman Shallan

Zagazig University

Hassan M. Maaly

Zagazig University

Mohammed M. Elgiar

Zagazig University

Alaa El-Din Elsisī (✉ elsisiae@missouri.edu)

University of Missouri <https://orcid.org/0000-0001-8190-6100>

Research Article

Keywords: Energy Dissipation, Hysteretic Behavior, Steel Wall, Seismic Behavior, Finite Element

Posted Date: April 15th, 2021

DOI: <https://doi.org/10.21203/rs.3.rs-412796/v1>

License:  This work is licensed under a Creative Commons Attribution 4.0 International License.

[Read Full License](#)

Abstract

Currently, the steel plate shear wall (**SPSW**) is commonly used in high-rise steel buildings as a lateral load resisting system. The **SPSW** consists of the boundary frame and infill plate. The objectives of this work are to study the effect of same weight different infill plate types, the effect of boundary frame characteristics, and the effect of infill plate weld separation on the seismic behavior of the **SPSWs**.

A numerical method was proposed to have a comprehensive comparison of seismic behaviors of different types of **SPSWs**, having the same weight. The model was validated by using previously published numerical and experimental works. The study covers unstiffened (**USPSW**), stiffened (**SSPSW**), and corrugated steel plate shear wall (**CSPSW**). Similarly, the effect of boundary frame stiffness and welding separation characteristics between the plate and boundary frame will be studied, and key issues, such as load-carrying capacity, stiffness, and energy-dissipation capacity were discussed deeply. It was found that the **SSPSW** has better seismic behavior than **USPSW** and **CSPSW**. **SSPSW** has a higher load-carrying capacity than **USPSW**, and **CSPSW** by about 14, 24%, respectively. **USPSW** is more sensitive to the stiffness of the boundary frame than **CSPSW**. The plate welding separation has a greater impact on the initial stiffness than load-carrying capacity. When plate-column welding separation occurs, the initial stiffness, and the energy dissipation capacity reduces by about 21%, and 14%. Whereas, when the plate-beam separation occurs, the initial stiffness and energy dissipation capacity reduce by about 36%, and 20.5%.

Introduction

The steel plate shear wall consists of a boundary frame, fish plate, and infill panel, as shown in Fig. 1 a). The steel plate shear wall is commonly used in high-rise steel buildings as a lateral load resisting system. Steel plate shear walls (**SPSW**) are preferred by designers due to many advantages such as lightweight, easy construction, and reduced structure reactions. **SPSW** is a lateral load resisting system with high lateral strength, initial stiffness (K_1), and shear performance, (Youssef et al. 2010; Yousuf and Bagchi 2010).

The **SPSWs** can be classified as follows:

- Unstiffened steel plate shear wall (**USPSWs**).
- Stiffened steel plate shear wall (**SSPSWs**).
- Composite steel plate shear wall (Rafiei et al. 2015).
- Corrugated steel plate shear wall (**CSPSWs**).

The **CSPSWs** can be classified according to the corrugation direction as follows:

- Horizontal corrugated steel plate shear wall (**HCSPSWs**).
- Vertical corrugated steel plate shear wall (**VCSPSWs**).

Figure 2 shows the plate geometry and configuration of **USPSWs**, **SSPSWs**, **HCSPSWs**, and **VCSPSWs**.

According to AISC Design Guide 20 (AISC 2016), the load-carrying capacity of the wall panel in **USPSW** is given by Eq. 1.

$$V_{m, PW} = 0.5 f_y t_w L_{CF} \sin 2\alpha \quad \text{Eq. (1)}$$

Where, $V_{m, PW}$ is the maximum load-carrying capacity of the plate, f_y is yielding strength of the steel material, t_w is the thickness of wall panel, L_{CF} is the clear distance between column flanges, and α is the angle of inclination of the tension field from the vertical direction, permitted to be taken as 40° .

According to the Design Manual for PC bridges with corrugated steel webs for deeply corrugated web panels, the critical shear stress τ_{cr} equals the shear yielding stress τ_y , and then lateral strength of the wall panel in **CSPSW** with deep corrugation could be given by Equation 2

$$V_{m, CW} = \tau_{cr} t_w L_{CF} \quad \text{Eq. (2)}$$

Where, $V_{m, CW}$ is the maximum load-carrying capacity of the corrugated panel, τ_{cr} is the critical shear stress equals the shear yielding stress τ_y , t_w is the thickness of the wall panel, L_{CF} is the clear distance between column flanges. The shear yielding stress τ_y could be determined by the Von Mises yielding criterion shown in Eq. 3.

$$\tau_y = \frac{f_y}{\sqrt{3}} \quad \text{Eq. (3)}$$

Although **USPSW** reaches to yield under a low level of lateral displacement, **USPSW** still has a high load-carrying capacity after buckling of infill panel. This can be attributed to the phenomena of the tension field (Caccese et al. 1993; Guo et al. 2015; Wang et al. 2015), which can dissipate the input energy by acting as a plastic hinge in the yielded infill panel. **USPSW** has a height to thickness ratio λ greater than 150, as a result, when a small drift is applied out-of-plane deformation occurs. Then, the tension fields of the thin plate are formed. Tension field theory describes the high out-of-plane buckling of thin plates, which are subjected to planar displacements. **CSPSW** is a good choice to avoid complex construction processes for welding stiffeners or casting concrete on site. Corrugations represent ribs, which increase the axial and out-of-plane bending stiffness along the direction parallel to ribs and decrease the axial and out-of-plane bending stiffness along the direction perpendicular to ribs; known as Accordion Effect (Shon et al. 2017; Zhao et al. 2017). This means that vertical **CSPSW** (**VCSPSW**) resists vertical loads more than horizontal **CSPSW** (**HCSPSW**), and **HCSPSW** resists lateral shear more than **VCSPSW**.

Several works were conducted on the **SPSW** system to improve its seismic behavior, load-carrying capacity, and energy dissipation capacity (Thorburn et al. 1983; Caccese et al. 1993; Driver et al. 1998; Hitaka and Matsui 2003a; Alinia and Dastfan 2007; Choi and Park 2009; Li et al. 2009; Vian et al. 2009; Chen and Jhang 2011; Alavi and Nateghi 2013a; Nie et al. 2013a; Paslar et al. 2020).

Some works focused on the seismic performance of **USPSW**. It was found that thin **USPSW** can achieve high post-buckling strength and good seismic behavior, which can be attributed to tension field action. Using thin **USPSW** instead of thick **USPSW** produces early tension field action that can dissipate more energy by acting as a plastic hinge (Thorburn et al. 1983). Single-span three-story **USPSW** was experimentally studied (Caccese et al. 1993). It was found that the thickness of the infill panel has a great influence on seismic behavior (Caccese et al. 1993). A cyclic test of four-story thin **USPSW** was conducted (Driver et al. 1998); the results showed good seismic performance, as story drift reached 4% before reached to failure and high energy dissipation capacity. Other works focused on the infill plate interconnection with the boundary frame. The infill plate interconnection effects on the structural behavior of steel plate shear walls were numerically studied (Paslar et al. 2020). The behavior of the partially connected plates with different interconnections types was compared to the fully connected infill plate. It was found that a system with an 80% connection between infill plate with boundary elements has a lower load-carrying capacity, stiffness, ductility, and energy-dissipation capacity than a fully-connection system. Although partially connected plates showed effects on the wall performance, the simulation of actual separation due to cracks was not involved in that study.

A lot of studies focused on using **SSPSW** to improve seismic behavior (Hitaka and Matsui 2003b; Alinia and Dastfan 2007; Cao et al. 2008; Li et al. 2009; Alavi and Nateghi 2013b; Guo et al. 2017).

Due to the favorable performance of the corrugated webs in the analysis and design of bridge plate girders, researchers started to utilize them in the **SPSW** as an infill plate. The application of corrugated plates as the web of steel coupling beams was investigated (Shahmohammadi et al. 2013). It was found that using the corrugated web could achieve more rotation capacity than common steel coupling beams. An equivalent classical plate model of corrugated structures was proposed and studied (Ye et al. 2014). Other studies were conducted on shear buckling and buckling tendency (Yi et al. 2008; Moon et al. 2009; Ye et al. 2014).

Due to its construction and structural performance advantages over the **USPSW**, many researchers moved toward studying the performance of **CSPSW** (Emami and Mofid 2014; Bahrebar et al. 2016; Dou et al. 2016; Shon et al. 2017). It was found that the energy dissipation capacity, ductility ratio, and the initial stiffness of the **CSPSW** are approximately 52%, 40%, and 20% greater than **USPSW** (Emami and Mofid 2014; Vigh et al. 2014). Shear buckling deformation of corrugated metal was studied, and an equation to calculate the global shear buckling of corrugated metal was proposed (Easley and McFarland 1969). An experimental study on the shear hysteresis behavior of CSPSWs was conducted (Shon et al. 2017). It was found that CSPSWs have good seismic behavior, high carrying moment capacity, energy dissipation capacity, and high initial stiffness.

In addition to experimental results, numerical methods were used in the analysis of **SPSW** (Dou et al. 2016). Results showed that repeating the number of corrugations has a great effect on lateral strength. Comparative studies were conducted on the shear buckling behavior of trapezoidal and sinusoidal corrugated steel plates (Zhao et al. 2017). It was found that sinusoidal corrugation has slightly greater lateral strength than trapezoidal corrugation with the same fold length.

Although a lot of research works focus on the behavior of the **USPSWs**. This paper has two main purposes; The first purpose is to perform a comparative study to investigate the different behaviors of the

wall with infill plates that have different types and the same weight per unit area. The second purpose of this study is to investigate the effect of welding separation that can happen due to aging, cyclic load due to wind or fabrication deficiency, and its effect on the hysteretic and other behaviors will be investigated. This paper studied more parameters such as infill plate type, boundary frame stiffness, and welding separation characteristics for **USPSWs**, **CSPSWs**, and **SSPSW**, which have the same weight, under cyclic loading test Fig. 1.c. The cyclic nonlinear behavior of **CSPSWs** and **SPSWs** was studied. Finite element models were developed by using **ABAQUS** software. Experimental and numerical works from the literature were used to validate the finite element model. Different seismic behavior, load-carrying mechanism, load-carrying capacity, hysteretic behavior, and energy dissipation capacity were analyzed and compared for different parameters. Two main topics were focused on this paper; the first topic is the seismic behavior of different kinds of **SPSWs**, having the same weight. The second topic is the effect of welding separation between the infill plate and the boundary frame.

Problem Description

A typical two groups of thin **USPSW**, **SSPSW**, and **CSPSW** systems were modeled using **ABAQUS** software. The first group represents the strong boundary frame case (denoted as **S**), and the second group represents the weak boundary frame case (denoted as **W**). The parametric study includes the effect of panel type, stiffness of boundary elements, and welding separation characteristics. Panel type can be plane (**P**), stiffened, or sinusoidal corrugated panel. The sinusoidal corrugation direction can be horizontal (**H**) or vertical (**V**). In this study, for the case of stiffened panels, only horizontal stiffeners case (**HS**) will be studied.

In the strong case, the boundary elements were designed according to AISC Design Guide 20 (Sabelli and Bruneau 2006; ANSI/AISC 341 – 10 2010). The beam section was **HM500×300×11×15** similar to **W21×68**, and the column section was **HW400×400x13X21** similar to **W14X132**.

The samples were as following:

- **SPt5**, **SPt6.75** represent the strong cases of the plane with thickness 5, 6.75 mm, respectively.
- **Sht5**, **Svt5** represents the strong cases of the horizontal and vertical corrugated panel.
- **SPt5-HS** represents the strong cases of the stiffened plane steel shear wall.

The models of **SPt6.75**, **Sht5**, **Svt5**, and **SPt5-HS** have the same weight per unit area. Figure 3 shows the geometry of the strong case **SPt5** & **SPt6.75**, **Sht5**, **Svt5**, and **SPt5-HS**.

In the weak case, the boundary frame was 40% lower bending stiffness than the strong case. The beam section was **HM400×300×10×16** equivalent to **W16×67** and the column section was **HW350×350×12×19** equivalent to **W14×90**. Wall panels had a height of 3000 mm, a span of 3000 mm, and a thickness of 5 mm.

The samples were as following:

- **WPt5** represents the weak cases of the plane wall.
- **WHt5**, **WVt5** represent the weak cases of the horizontal, vertical corrugation walls, respectively.
- **WPt5-HS** represents the weak cases of the stiffened plane steel shear wall.

All the models of **WHt5**, **WVt5**, and **WPt5-HS** have the same weight per unit area. Figure 1d) shows the section of stiffeners used in **SPt5-HS** and **WPt5-HS**. The height of the stiffeners was 120 mm. The stiffener flange was 60 mm, and the thickness of the stiffeners was 5 mm. Figure 4 shows the geometry of weak case **WPt5**, **WHt5**, **WVt5**, and **WPt5-HS**.

Additional models were created to study the effect of welding crack/separation.

The Models were as following:

- **PS1** and **PS2** represent the plate welding separation with one column and beam, respectively. The separation length was 3000 mm (whole length).
- **PS3** represents corner beam separation with a length of 1000 mm.
- **PS4** represents middle beam separation with a length of 1000 mm.
- **PS5** represents corner beam separation with a length of 2000 mm.

Figure 5 provides the details for **PS1**, **PS2**, **PS3**, **PS4**, and **PS5**, including plate welding separation lengths and locations used in this parametric study.

The location weld separation can happen randomly due to the effect of aging deterioration. The separation due to the vertical and horizontal load happens at the location of stress concentrations. A preliminary study was done to investigate the separation length that can provide a significant effect on the wall behavior. The model **PS1**, **PS2** studied the effect of plate Colum, and Beam full separation to know which element separation has more effect on the **USPSW** seismic behavior. It was observed that **USPSW** is more sensitive to beam welding separation than column welding separation, so the effect of plate-beam welding separation was studied deeply in the models **PS3**, **PS4**, and **PS5**. The models **PS3**, **PS4** studied the effect of beam separation location to know which location has an obvious effect on the seismic behavior. The model **PS3** studied the plate corner separation, where tension fields start to form. The model **PS4** studied the plate middle separation as the maximum out-of-plane deformation occurs at the plate center. The separation length was one-third of the plate width. The model **PS5** represents a combination of plate corner and middle separation.

All walls have the same width and height and the same aspect ratio (Ratio) of one. The wavelength of the corrugation is 300 mm, with a 60 mm amplitude, as shown in Fig. 1b). The **VCSPSWs** and **HCSPSWs** have the same wavelength, amplitude, and corrugation with different directions of the corrugated panel, i.e., **H** or **V**. The **USPSW** with stiffeners had the same weight as the **CSPSW**. The difference between the fold length (the original length of the corrugated panel before corrugation) and panel length determines the stiffener's size. The parametric case study is shown in **Table 1**.

FINITE ELEMENT MODELING

To study the nonlinear behaviors of **USPSW**, **SSPSW**, and **CSPSW**, accurate finite element analysis should be conducted. The boundary frame and infill panel were modeled using quadrilateral shell elements (**S4R**), to avoid shear locking phenomena (Tessler and Spiridigliozzi 1988; Abaqus et al. 2013). Shear locking phenomena can be defined as the unintentional generation of shearing deformation rather than the desired bending deformation. Therefore, the element becomes too stiff and the overall deflections are lesser. This phenomenon could have happened mainly with fully integrated, first order, solid linear elements subjected to bending loads. It can be avoided by using higher-order elements like quadratic elements and do not use the linear elements if there is a bending load. Therefore, quadrilateral shell elements with reduced-integration (**S4R**) were used (Abaqus et al. 2013).

Structural modeling, mechanical properties of materials, the boundary condition of models, and time history of loading and initial defect are presented in detail as follows.

Mechanical Properties of Steel Materials

For the parametric study, the boundary frame steel and the infill panel materials have a yielding strength of 345 MPA and 235 MPA, respectively. The materials elastic modulus $E = 206000$ MPA, Poisson's ratio $\nu = 0.3$ and hardening modulus $E_h = E/100$. The four-node shell element S4R with reduced integration was used for the modeling of all members. Material and geometric nonlinearity was taken into consideration in the analysis. After the material reaches to yield point, the response of the system becomes nonlinear and irreversible. Moreover, the response of the material under cyclic and monotonic loading is different; therefore, material nonlinearity should be taken into consideration (Shi et al. 2011). Due to changes in geometric out-of-plane deformation of the system during the loading process, reciprocating two-way tension fields snapped through the shape of the corrugated panel and zero or negative stiffness phenomena, the geometric nonlinearity should be taken into consideration. The isotropic hardening behavior was considered (Abaqus et al. 2013).

Modal Analysis and Initial Defect

The initial defect of out-of-plane or out-of-plane initial imperfection, which may occur due to the manufacturing process, storage, and installation process, should be taken into consideration in the cyclic analysis as it might affect the plate strength. Initial imperfection was set as 1/1000 of the plate length in the previous researches of the thin **USPSW**. Due to the higher out-of-plane stiffness of **CSPSW**, initial imperfection was set as 1/750 of panel height in this study (Nie et al. 2013b). **ABAQUS** command "Imperfection" was used to modify the coordinates of plate nodes using major buckling modes. The eigenvalue buckling analysis was used to evaluate the imperfection distribution over the panel by multiplying the first buckling mode by the scale factor.

Boundary Conditions and History Loading

The nonlinear cyclic analysis was conducted on groups of thin **USPSW** (e.g. **SPT6.75**, **SPT5**, **WPT5**, **PS1**, **PS2**, **PS3**, **PS4**, and **PS5**), **CSPSW** (e.g. **SHt5**, **SVt5**, **WHT5**, and **WVt5**), and **SSPSW** (e.g. **SPT5-HS**, and **WPT5-HS**). The lateral displacement was applied on the exterior column flange on the top right panel zone. The lateral displacement was increased gradually to produce drift ratios of 0.25%, 0.5%, 1%, 1.5%, 2%, 2.5%, 3% and 4%. Each amplitude was repeated twice, as shown in Fig. 1c). The column base region had a fixed boundary condition, in which all these nodes were restrained in all the six degrees of freedom. To prevent the out-of-plane buckling of the whole system, the out-of-plane displacement for the nodes of the beam centerline and all nodes of the column and beam connections were constrained. These constraints consider the out-of-plane bracing provided by the floor system.

Experimental Work Details and Numerical Model Validation

To verify the accuracy of numerical simulation, previously published quasi-static test results were used (Park et al. 2007; Zhao et al. 2017). Finite element models were created, and the hysteretic curves were compared to the experimental results.

Experimental work Validation

Tested Specimens

Five **USPSW** specimens with a single bay and three stories were tested where the specimen **SC4T** was selected for validation in this study (Park et al. 2007). The height, width, and thickness of the plates were 1000 mm, 1500 mm, and 5 mm, respectively. The section of the internal beams was **H200×200×16×16** mm, and the top beam and the columns sections were **H400×200×16×16** and **H250×250×20×20**, respectively. The detailed dimensions of the specimen are shown in Fig. 6a).

Numerical simulation

The material of infill panels and boundary elements was steel **SM490** with yield stress $F_y = 330$ MPa. The Chaboche constitutive model (Chaboche 1986, 1989) is adopted; therefore, the combined hardening behavior was considered (Abaqus et al. 2013). This rule should be determined to perform a cyclic analysis and predict deformation behavior. A combined hardening model includes isotropic and nonlinear kinematic hardening rules. This model was firstly summarized by (Chaboche et al.). In the model, two parameters for isotropic hardening (i.e. Q_∞ and b), and eight parameters for nonlinear kinematic hardening containing four back stresses (i.e. $C_1, \gamma_1, C_2, \gamma_2, C_3, \gamma_3, C_4, \gamma_4$). Cyclic stress versus strain curve should be required to determine the isotropic hardening parameters Q_∞ and b . Therefore, Q_∞ can be determined from the difference between cyclic and monotonic stress versus strain curves. The value of b can be determined from the fitting of peak stresses for each cycle. Whereas the parameters of nonlinear kinematic hardening model can be determined from hysteretic loop data from strain-controlled round bar tensile tests (Ryu et al. 2018). Several cyclic hardening parameters of the material should be assigned such as the kinematic hardening modulus (C), the rate at which hardening modulus decreases with the plastic strain (γ), the maximum change in the size of the yield surface (Q_∞), and is the rate at which initial yield stress change with the plastic strain (b) (Abaqus et al. 2013). The cyclic hardening parameters of

the material are shown in Table 2. **S4R** elements were used to simulate the boundary frame and infill panel. The bottom of the model had a fixed boundary condition, and the initial out-of-plane defect was selected 1/1000 of the steel plate height. The cyclic loading process is shown in Fig. 2a) where the loading test was applied using the reference point in the middle of the upper beam until the system is destroyed completely.

Results And Discussion

The deformed shape of the present finite element model for the sample **SC4T** is found in **Figure 6 b)**. Besides, the load-displacement curves for the experiment test, previous and present **FEM** results can be seen in **Figure 6 c)** (Zhao et al. 2017). The previous finite element modeling shows differences in the maximum lateral capacities of about 7% and 9% in the positive and negative direction and some differences in hysteretic behavior. However, the present numerical simulation shows hysteretic behavior similar to the experimental results with a difference in the load-carrying capacity of 4%. The reason for the bigger difference between previous simulation and experimental results was the absence of a cyclic hardening parameter in the definition of material. It can be concluded that the current numerical simulation technique can be used to predict the nonlinear behavior of **SPSWs**.

Numerical Work Validation

Another validation for this modeling technique was performed by using a previously published numerical study (Zhao et al. 2017). In that study, eight **USPSW** models with single-bay and one floor were studied (Zhao et al. 2017). The models **SC-PW** and **SC-HSW** were selected for the validation of the current **FEM**. The **FEMs** geometry and configurations are shown in **Figure7 a)** and **b)**. The wall dimensions were **3000×3000×5 mm**, the length of the corrugation wave was 300 mm, and the amplitude was 60 mm. The boundary column's section was **HW400×400×13×21 mm**, and the top beam's section was **HM500×300×11×15 mm**. The material of the infill panel has a yield strength of 235 MPa, while the boundary frame material has a yield strength of 345 MPa, with an elastic modulus $E = 2.06$ GPa, a Poisson's ratio $\nu = 0.3$, and hardening modulus $E_h = 1/100E$. For **SC-PW**, the present **FEM** had initial stiffness greater than the previous FEA by about 3% and by about 4.4% higher load-carrying capacity, as shown in **Figure 7 c)**. For **SC-HSW**, the present simulation had less initial stiffness than the previous simulation by about 0.7% and by about 3.7% less load-carrying capacity, as shown in **Figure 7 d)**. The current finite element modeling results have good agreement with the previously published works.

EFFECT OF PANEL TYPE AND DIRECTION OF CORRUGATION

To show the effect of panel type and direction of corrugation on the seismic behavior, the results of models **SPT5**, **SHT5**, **SVt5**, **SPT5-HS**, and **SPT6.75** will be compared and discussed. Models **SHT5**, **SVt5**,

SPT5-HS, and **SPT6.75** have the same weight for comparison reasons. The nonlinear cyclic analysis was conducted on the five models, and the hysteretic behavior was recorded.

Hysteretic behavior of strong **SPSW** walls **SPT5**, **SVt5**, **SHT5**, **SPT5-HS**, and **SPT6.75** are shown in **Figure 9**, in which the drift ratio is presented on the x-axis (%) and load-carrying capacity is presented on the y-axis (kN). The hysteretic curves show that panel type and corrugation direction have an obvious effect on hysteretic behavior. From **Figure 9 a)**, it is clear that **SHT5** has a higher load-carrying capacity than **SPT5** in the early stages up to $\pm 1.5\%$ drift. After **SHT5** reached peak lateral strength, plastic buckling occurred. Therefore, the load-carrying capacity of **SHT5** is degraded faster than the case of **SPT5**, which uses tension field action to have high post-buckling lateral strength. Also, **Figure 9 a)** shows the reduction of reloading stiffness, which can be attributed to the plastic deformation caused by the loading, unloading, and reloading in the opposite direction.

Figure 9 b) shows that both **SPT5-HS** and **SPT5** have the same lateral strength mechanism, which depends on tension field action; this action produces post-buckling load capacity. The results show that **SPT5-HS** achieves plumper hysteresis behaviors and stiffness than **SPT5**. **Figure 9 c)** indicates that when the span-to-height ratio, panel thickness, and the boundary frame remain the same, corrugation direction has a significant effect on load-carrying capacity. **SHT5** has a higher load-carrying capacity than **SVt5** in the early stages. This might be attributed to the accordion effect, which means that the horizontal corrugations represent horizontal ribs, which resist lateral displacement. After **SHT5** reached the yield, plastic buckling occurred in the panel; therefore, the load-carrying capacity of **SHT5** became the same as **SVt5**. In general, **Figure 9 a), d), and e)** indicate that with the same weight, **CSPSW** has different lateral strength mechanisms than plane infill **USPSW** or **SSPSW**.

Figure 9 d) shows a comparison between the hysteretic behavior of **SHT5** and **SPT5-HS**, which have the same weight. **Figure 9 d)** shows that **SPT5-HS** has better seismic behavior than **SHT5**, hence after **SHT5** reached peak load-carrying capacity, at lateral story drift $\pm 1\%$, plastic deformations, and local buckling occur in the system. **SHT5** load-carrying capacity starts to degrade faster, while **SPT5-HS** load-carrying capacity increases depending on tension field action. **Figure 9 e)** shows a comparison between the hysteretic behaviors of **SHT5** and **SPT6.75**, where both of them have the same weight. **Figure 9 e)** shows that **SPT6.75** has better seismic behavior than **SHT5**. As, **SHT5**'s load-carrying capacity decreases after reaches to the peak capacity at lateral drifts $\pm 1\%$, while **SPT6.75**'s lateral load capacity increases up to lateral drifts $\pm 4\%$.

The backbone curves can be obtained from the hysteretic curve in both pull and push directions, as shown in **Figure 9 f)**. For each drift, the highest load-carrying capacities for the first cycle were extracted from the hysteretic curves in both directions to form the backbone curves (Zhao et al. 2017). The initial stiffness (K_1), the second cyclic stiffness (K_2), load-carrying capacity, yield points, and maximum points can be evaluated from backbone curves, as shown in **Table 3**. Here, the K_1 , K_2 stiffness is the system stiffness at drifts of 0.25, 0.5%, respectively. It can be calculated by Eq. (1) (Nie et al. 2008). The yield point Y is a point at which local buckling and plastic deformations appear in the system, which can be

identified with the commonly used “Equivalent area method”. Where Δ_y is the yield displacement, V_y is the yielding force, Δ_m is the displacement at the maximum load-carrying capacity, and V_m is the maximum load-carrying capacity.

From **Figure 9 f)** and **Table 3**, at the 0.5% drift in the push direction, it can be observed that the walls **SHt5**, **SVt5**, **SPt5-HS**, and **SPt6.75** have higher K_2 stiffness than **SPt5** by percentage values of 14.6, 15.6, 9, and 22.8%, respectively.

At story drifts of $\pm 4\%$, **SPt5** gives approximately the same load-carrying capacity of **SHt5** and **SVt5** which occurs at $\pm 1\%$ lateral drifts. At the 4% drift in the push direction, **SPt5-HS**, and **SPt6.75** have a higher load-carrying capacity than **SPt5** by about 23, and 7.5%, respectively. The case of **SPt5-HS** has the maximum increasing percentage value. Therefore, the horizontal stiffened wall has better seismic behavior than a horizontal corrugated wall, which has the same weight.

EFFECT OF BOUNDARY FRAME STIFFNESS

In this section, the influence of boundary element stiffness on the seismic behavior of **USPSWs**, **SSPSWs**, and **CSPSWs** will be studied deeply.

In this section, the hysteretic behaviors of corrugated steel plate wall, **USPSW**, and **SSPSW** with the weak case were compared with the strong case, as shown in **Figure 10 a-d)**. It can be found that a system with weak stiffness boundary elements has a 40% lower stiffness than the strong systems. The same cyclic behavior with lower lateral strength and lower initial stiffness was observed. **USPSW** and **SSPSW** showed more sensitivity for weak boundary elements. The effect of weak boundary elements on lateral strength is more obvious for the horizontal **HCSPSW** systems **SHt5** and **WHt5** than the **VCSPSW** systems **SVt5** and **WVt5**.

Backbone curves were extracted from hysteretic curves in pull and push direction for different models, as shown in **Figure 10 e)**. The K_i , K_2 stiffness, yield, and maximum points were extracted from backbone curves, as shown in **Table 4**, as discussed in the previous section.

From **Figure 10 e)** and **Table 4**, at the 0.5% drift in the push direction, it can be seen that reducing the boundary frame stiffness by about 40% causes K_2 stiffness degradation in the walls **WPt5**, **WHt5** and **WVt5**, and **WPt5-HS** by percentage values of 16, 7, and 8%, respectively. It can be concluded that **USPSWs** (i.e. **WPt5**) and **CSPSWs** (i.e. **WHt5** and **WVt5**) have the maximum and minimum reduction values, respectively.

At the 4% drift in the push direction, it can be observed that reducing the boundary frame stiffness causes load-carrying capacity degradation in the walls **WPt5**, **WHt5**, **WVt5**, and **WPt5-HS** by percentage values of 18, 12, 11, and 16%, respectively.

It can be concluded that the stiffness reduction of boundary members has a greater impact on load-carrying capacity than the stiffness of the system. Plane steel plate walls and stiffened steel plane walls are more sensitive to the effect of boundary frame stiffness reduction. **VCSPSW** is less sensitive to boundary frame stiffness reduction. This might be attributed to the that the vertical corrugations represent vertical ribs, which resist the frame action.

EFFECT OF WELDING SEPARATION CHARACTERISTICS

To study the impact of welding separation/crack on the lateral strength, energy dissipation capacity, and cyclic behavior, five **FEMs** with different welding separation characteristics were developed. As the plane wall, such as **USPSW**, was more sensitive to the boundary frame stiffness, the welding separation of the plane plate with the boundary frame was studied. The thicknesses of the plate and boundary frame elements remain the same as **SPT5** for comparison reasons. **Figure 5** shows the details of welding separation models **PS1**, **PS2**, **PS3**, **PS4**, and **PS5**, including the location and length of the separation.

Hysteretic Behavior and Backbone Curves of Systems with Welding Separation

The hysteretic curves of **SPT5**, **PS1**, **PS2**, **PS3**, **PS4**, and **PS5** were presented and compared in this section, as shown in **Figure 11 a-e)**. **Figure 11 a-b)** compares the hysteretic curve of wall **SPT5** to the column welding separation case **PS1**, and beam welding separation case **PS2**. It can be observed that the weld separation causes a reduction in the load-carrying capacity values for the cases **PS1** and **PS2** through the hysteretic relation. Also, the beam welding separation has a more significant effect on reducing the base shear than the column welding separation case. At 0.25% drift, the reduction percents for the case of **PS1** and **PS2** are 21% and 36% in push direction, respectively; similar behavior was observed in the pull direction. At the 4% drift in push direction, similar behavior was observed with reduction percentage values of 13% and 16% for **PS1** and **PS2**, respectively. It can be concluded that **USPSW** is more sensitive to beam welding separation than column welding separation, so the effect of plate-beam welding separation will be studied deeply.

Hysteretic curves of plate-beam welding separation models with different separation lengths, and locations **PS2**, **PS3**, **PS4**, and **PS5** were shown in **Figure 11 c-e)**. At 0.25% drift in push direction, the welding separation in cases **PS3**, **PS4**, and **PS5** caused a reduction in the load-carrying capacity by 20%, 20%, and 10% and at 4% drift, this reduction was 3%, 0%, and 4%, respectively. It can be concluded that, in the early stages of cyclic loading, the separation has a significant effect on the load-carrying capacity, and the effect is decayed by increasing the drift. At low values of drift, the wall mostly resists the shear force by the contact between the plate and the frame element, which makes the contact separation more effective. For high drift value, the tension field action starts at the non-separated part, and the dependency on the contact decreases. Besides, at the same separation length, the effect of separation is insignificant regardless of the location of the separation.

Backbone curves of **PS1**, **PS2**, **PS3**, **PS4**, and **PS5** were extracted from the hysteretic curves, as shown in **Figure 11 f**). Seismic behavior for different welding separation characteristics was evaluated using the loading function of **Fig. 1.c** and compared with the system without welding separation. Feature points were summarized from backbone curves, as shown in **Table 5**, using the method discussed in the first section. At the push direction, it can be found that welding separation affects the initial stiffness of the walls. The separation caused stiffness degradation in the walls **PS1**, **PS2**, **PS3**, **PS4**, and **PS5** by percent values of 21, 36, 20, 22, and 10%. The cases of full-beam separation and 2000 mm corner separation have the maximum and minimum reduction values. Both the case of 1000 mm separation in corner and middle approximately has the same reduction value. For the pull directions the reduction ratios were 21, 18, 18, 18, and 10% respectively and the second cycle stiffness reduction ratios were 30% 30% 6% 7% and 15%, respectively. It seems that the plate welding separation has more effect on the system stiffness than the load-carrying capacity (base shear). The **USPSW** system **is** more sensitive to plate-beam welding separation than plate-column. The plate-beam corner separation has a slightly greater impact on system strength than plate-beam middle separation, which reaches the same lateral strength at the drift ratio of 4%.

By comparing **PS1**, and **SPT5** backbone curves shown in **Figure 11 f**) considering Von-Mises stress distribution shown in **Figure 14, 15**, it can be observed that the right portion of the plate that is separated from the column does not undergo high-stress demands. The plate-column separation leads to fewer demand forces generated by tension field action on the column. As a result, a smaller column section is required. It can be observed a large stress concentration at the beam-column joint areas in the left portion of the plate that is connected to the boundary column, which should be designed for.

For the **PS2** model, it can be seen that the concentration of the stress in plate-boundary connection areas. This might be attributed to incomplete tension field action leading to the partially plate's post-buckling load-carrying capacity. The forces generated by incomplete tension field action and gravity loads are concentrated at the columns, producing large demand forces, which the boundary columns should be designed for. While, the top portion of the plate, which is separated from the top beam, does not undergo high-stress concentration. As a result, a smaller top beam section is required.

For partially plate-beam separation (i.e. **PS3**, **PS4**, and **PS5**), it can be observed that the separated portion does not undergo significant high-stress demands. Incomplete tension field action was observed, which leads to the partial plate's post-buckling load-carrying capacity.

In general, the partially plate-beam separation (**PS4**, **PS5**) could negatively increase the stresses at the connected column-beam joint areas leading to higher possibilities of early failure under seismic load. High demands due to diagonal tension field action at connected joint, which should be designed for. Increasing the separation length leads to a large increase in stress concentrations at the connecting portions.

Properties Degradation and Energy Dissipation Capacity

Lateral strength degradation reflects plastic buckling, out-of-plane deformation of infill panel, local failure in columns, and the damage occurs in different models under the same lateral displacement. In this study, the strength degradation coefficient (η) can be defined as (the ratio between the second and the first cycle load-carrying capacity at the same drift ratio).

Figure 12 a) shows the lateral strength degradation coefficient (η) for **USPSWs (i.e. SPt6.75, SPt5)**, **CSPSWs (i.e. SHt5, SVt5)**, **SSPSWs (i.e. SPt5-HS)**; it can be found that the η are varying between 0.85 and 1.0 except the second cycle of **SPt5** and **SPt6.75**, where the lateral strength degradation is about 0.8. This happens due to the initial yielding of the plane infill panel, which reduces the load-carrying capacity of the wall. The strength degradation coefficient (η) for **CSPSW** systems is higher than the **USPSW** system. This happens due to the efficient tension field action forms in opposite directions in the **USPSW**. Although the tension field action is formed in the corrugated panel, it is less effective due to the initial corrugation of the sheet.

The cyclic stiffness (K_i) describes the stiffness degradation for the different models. K_i can be calculated by the method described in (Nie et al. 2008) as below;

$$K_i = \sum_{i=1}^n P_j^i / \sum_{i=1}^n \Delta_j^i \quad \text{Eq. (4)}$$

Where, P_j^i is peak load-carrying capacity in each cycle and Δ_j^i is peak displacement for each cycle drift.

Figure 12 b) shows the stiffness degradation for **USPSW**, **SSPSW**, and **CSPSW**. It can be seen that stiffness degradation decreases steadily during the cyclic loading process. **SPt6.75** sample has higher initial stiffness than other samples. After the drift of $\pm 1\%$, the stiffness decreases below the **SSPSW** case. On the other hand, **SPt5** has the least cycle stiffness than other models.

Energy dissipation capacity reflects the seismic performance of the lateral resisting system. The energy dissipation capacity for each cycle is equal to the enclosed area of each hysteretic curve. The system with a plumper hysteretic curve has more energy-dissipation capacity. **Figure 13 a)** shows the accumulated energy dissipation capacity for different panel types with the strong case during cyclic number $N=12$. From **Figure 13 a)**, it is clear that the energy-dissipation capacities of **SPt6.75**, **SHt5**, **SVt5**, and **SPt5-HS** are higher than the case of **SPt5** by 14%, 29%, 32%, and 50%, respectively. **SVt5** has slightly greater energy dissipation than **SHt5**. The cases of **SPt5-HS** and **SPt6.75** have the maximum and minimum increasing values, respectively.

Figure 13 b) shows the accumulated energy dissipation capacity for **USPSW**, **CSPSW**, and **SSPSW** with different frames during cyclic number $N=12$. Similar to the strong case, **SSPSW**, and **CSPSW** still have

more energy-dissipation capacity than **USPSW** with the weak case. From **Figure 13 b)**, it can be concluded that reducing boundary frame stiffness by about 40% causes energy-dissipation capacity degradation in the walls **WPt5**, **Wht5**, **Wvt5**, and **Wpt5-HS** by percentage values of 18, 15, 12, and 12%, respectively.

This means that the accumulated energy dissipation of **USPSW** is more sensitive to the frame stiffness than **CSPSW**, and the **VCSPSW** is less sensitive to the frame stiffness than **HCSPSW**.

Figure 13 c) shows the accumulated energy dissipation capacity for the walls with welding separation **PS1**, **PS2**, **PS3**, **PS4**, and **PS5** during cyclic number **N=16**. It can be concluded that welding separation has a significant effect on the system's energy-dissipation capacity. The separation caused energy-dissipation degradation in the walls **PS1**, **PS2**, **PS3**, **PS4**, and **PS5** by percentage values of 14, 21, 3.3, 2.9, and 9%. The cases of the full and middle beam separation have the maximum and minimum reduction values, respectively. The plate-beam corner separation has a slightly greater impact on system energy-dissipation capacity than middle separation.

COMPARISON BETWEEN SYSTEMS FAILURE MODES

Figures 14 and 15 show the different failure modes for the systems. From **Figure 14**, it can be seen that the different details can change the deformed shape and failure mode of the models. Due to the cyclic loading process, two-way tension strips appear, and obvious out-of-plane deformation occurs. For plane **SPSW**, i.e., **Spt5**, **Wpt5**, and **Spt6.75**, clear two-way tension strips occur, and local buckling occurs at the top and bottom of boundary columns. For **CSPSW** with a horizontal corrugated sheet, i.e., **Sht5**, **Wht5**, no clear tension field strips form, and local buckling occurs at the bottom of columns. The maximum deformations occur at the vertical centerline. The maximum out-of-plane shear buckling for **Svt5** and **Wvt5** occurs at the horizontal centerline. Using a vertical corrugated steel plate lessens the impact of shear deformation on the boundary columns. For **Spt5-HS** and **Wpt5-HS**, local failure occurs at the bottom and top of columns. The out-of-plane deformation was effectively restrained by stiffeners. When plate-column welding separation occurs at **PS1**, local failure was not observed at the top of the column, whose welding was separated, **Figure 15**. It can be concluded that plate-column separation lessens the impact of tension strips on the column. The plate-beam welding separation model **PS2** has local buckling at the top and the bottom of the columns. The top beam did not provide an anchor for tension strips, due to welding separation. High out-of-plane deformations were observed at the top of the plate. The models with partially plate-beam welding separation, i.e., **PS3**, **PS4**, and **PS5**, showed local buckling at the top and bottom of the columns. Welding separation progress was observed, as shown in **Figure 15**.

Conclusion

In this paper, nonlinear cyclic analyses were conducted using numerical simulation for **USPSW**, **SSPSW**, and **CSPSW**. The effects of panel type, the direction of corrugation, boundary frame stiffness, and welding separation on initial stiffness, load carrying, energy, and dissipation capacities were investigated.

Two main topics were focused on this paper; the first topic is the seismic behavior under different kinds of infill walls with the same unit weight. The second topic is the effect of welding separation between the infill plate and the boundary frame.

- Finite element models were created and validated with published experimental and numerical works. The models were able to predict the previous results with a percentage error of 4%. It was found that **HCSPSW** has 15% and 11% higher stiffness at a drift ratio of 0.5% in the push and pull directions, respectively, and 29% higher energy dissipation than **USPSW**. It also has a higher lateral load-carrying capacity than vertical corrugation by about 4.3% in the pull direction. **VCSPSW** has a higher energy dissipation capacity than **USPSW** by about 32%.
- At the lateral story drift of 0.5%, The stiffness of **SSPSW** with **U120** stiffeners is higher than the **USPSW** with about 9.2%. **SSPSW** also has 23% and 24.5% higher lateral strength than **SPSW** and 34.6% and 23.7% higher than horizontal **CSPSW** in the push and pulls directions, respectively. It also has higher energy dissipation energy than **USPSW** by about 50%. **USPSW** is more sensitive to boundary element stiffness than **CSPSW**, and **VCSPSW** is less sensitive to weaker frames than **HCSPSW**.
- The reduction of the boundary frame stiffness has a greater impact on load-carrying capacity than the initial stiffness, while the plate welding separation has more influence on the system stiffness than the lateral strength. The separation has a significant effect on seismic behavior in the early stages of cyclic loading, as the walls mostly resist the shear force by plate-boundary frame contact before tension fields start at the non-separated part. When the plate-column welding separation occurs, the initial stiffness, lateral strength, and energy dissipation capacity reduce by about 21%, 13%, and 14%, respectively. While, the system with the plate-beam separation has lower initial stiffness, base shear capacity, and energy dissipation capacity than the system without separation by about 36%, 16%, and 20.5%, respectively. The **USPSWs** system is more sensitive to the plate-beam separation than the plate-column, especially the corner plate-beam separation.
- At the same infill plate weight per unit area, **SSPSW** has better seismic behavior than **USPSW** and **CSPSW**. **SSPSW** has a higher load-carrying capacity than **USPSW**, and **CSPSW** by about 14, 24%, respectively. It is recommended to use the **SSPSWs** system instead of **USPSWs**, and **CSPSWs** to improve the seismic behavior of the buildings.
- For engineering applications, during low cyclic drift ratio levels up to 0.5%, **USPSW** would be better to use, **CSPSW** would be preferred to use during medium cyclic drift ratio levels (0.5-1%). During high cyclic drift ratio levels, **SSPSW** would be preferred to use.

Declarations

Funding

Not applicable

Conflicts of interest/Competing interests

The authors have no affiliation with any organization with a direct or indirect financial interest in the subject matter discussed in the manuscript

Availability of data and material

All the used data and materials are included in this manuscript.

Code availability

Not applicable

References

- Abaqus, Simulia DS, Fallis A., Techniques D (2013) Abaqus Analysis User's Guide (6.14). Abaqus 612. <https://doi.org/10.1017/CBO9781107415324.004>
- AISC (2016) ANSI/AISC 341-16, Seismic Provisions for Structural Steel Buildings. Seism Provisions Struct Steel Build. <https://doi.org/111>
- Alavi E, Nateghi F (2013a) Experimental study on diagonally stiffened steel plate shear walls with central perforation. J Constr Steel Res. <https://doi.org/10.1016/j.jcsr.2013.06.005>
- Alavi E, Nateghi F (2013b) Experimental Study of Diagonally Stiffened Steel Plate Shear Walls. J Struct Eng. [https://doi.org/10.1061/\(ASCE\)st.1943-541x.0000750](https://doi.org/10.1061/(ASCE)st.1943-541x.0000750)
- Alinia MM, Dastfan M (2007) Cyclic behavior, deformability and rigidity of stiffened steel shear panels. J Constr Steel Res. <https://doi.org/10.1016/j.jcsr.2006.06.005>
- ANSI/AISC 341-10 (2010) Seismic Provisions for Structural Steel Buildings. Am Inst Steel Constr. <https://doi.org/111>
- Bahrebar M, Kabir MZ, Zirakian T, et al (2016) Structural performance assessment of trapezoidally-corrugated and centrally-perforated steel plate shear walls. J Constr Steel Res. <https://doi.org/10.1016/j.jcsr.2016.03.030>
- Caccese V, Elgaaly M, Chen R (1993) Experimental Study of Thin Steel-Plate Shear Walls under Cyclic Load. J Struct Eng. [https://doi.org/10.1061/\(ASCE\)0733-9445\(1993\)119:2\(573\)](https://doi.org/10.1061/(ASCE)0733-9445(1993)119:2(573))
- Cao C-H, Hao J-P, Zhong W-H, et al (2008) Cyclic test of diagonal stiffened steel plate shear walls. In: Proceedings of the 10th International Symposium on Structural Engineering for Young Experts, ISSEYE 2008

- Chaboche JL (1986) Time-independent constitutive theories for cyclic plasticity. *Int J Plast.* [https://doi.org/10.1016/0749-6419\(86\)90010-0](https://doi.org/10.1016/0749-6419(86)90010-0)
- Chaboche JL (1989) Constitutive equations for cyclic plasticity and cyclic viscoplasticity. *Int J Plast.* [https://doi.org/10.1016/0749-6419\(89\)90015-6](https://doi.org/10.1016/0749-6419(89)90015-6)
- Chaboche JL, Van KD, Cordier G MODELIZATION OF THE STRAIN MEMORY EFFECT ON THE CYCLIC HARDENING OF 316 STAINLESS STEEL. *Trans Int Conf Struct Mech React Technol*
- Chen SJ, Jhang C (2011) Experimental study of low-yield-point steel plate shear wall under in-plane load. *J Constr Steel Res.* <https://doi.org/10.1016/j.jcsr.2011.01.011>
- Choi I-R, Park H-G (2009) Steel plate shear walls with various infill plate designs. *J Struct Eng.* [https://doi.org/10.1061/\(ASCE\)0733-9445\(2009\)135:7\(785\)](https://doi.org/10.1061/(ASCE)0733-9445(2009)135:7(785))
- Dou C, Jiang ZQ, Pi YL, Guo YL (2016) Elastic shear buckling of sinusoidally corrugated steel plate shear wall. *Eng Struct.* <https://doi.org/10.1016/j.engstruct.2016.04.047>
- Driver RG, Kulak GL, Kennedy DJ., Elwi AE (1998) Cyclic test of four-story steel plate shear wall. *J Struct Eng.* [https://doi.org/10.1061/\(ASCE\)0733-9445\(1998\)124:2\(112\)](https://doi.org/10.1061/(ASCE)0733-9445(1998)124:2(112))
- Easley JT, McFarland DE (1969) Buckling of light-gauge corrugated metal shear diaphragms. *J Struct Div ASCE*
- Emami F, Mofid M (2014) On the hysteretic behavior of trapezoidally corrugated steel shear walls. *Struct Des Tall Spec Build.* <https://doi.org/10.1002/tal.1025>
- Guo HC, Hao JP, Liu YH (2015) Behavior of stiffened and unstiffened steel plate shear walls considering joint properties. *Thin-Walled Struct.* <https://doi.org/10.1016/j.tws.2015.09.005>
- Guo HC, Li YL, Liang G, Liu YH (2017) Experimental study of cross stiffened steel plate shear wall with semi-rigid connected frame. *J Constr Steel Res.* <https://doi.org/10.1016/j.jcsr.2017.04.009>
- Hitaka T, Matsui C (2003a) Experimental Study on Steel Shear Wall with Slits. *J Struct Eng.* [https://doi.org/10.1061/\(ASCE\)0733-9445\(2003\)129:5\(586\)](https://doi.org/10.1061/(ASCE)0733-9445(2003)129:5(586))
- Hitaka T, Matsui C (2003b) Experimental study on steel shear wall with slits. *J Struct Eng.* [https://doi.org/10.1061/\(ASCE\)0733-9445\(2003\)129:5\(586\)](https://doi.org/10.1061/(ASCE)0733-9445(2003)129:5(586))
- Li F, Li H, Li Z-M, et al (2009) Cyclic test of diagonally stiffened steel plate shear wall. *Xi'an Jianzhu Keji Daxue Xuebao/Journal Xi'an Univ Archit Technol*
- Moon J, Yi JW, Choi BH, Lee HE (2009) Lateral-torsional buckling of I-girder with corrugated webs under uniform bending. *Thin-Walled Struct.* <https://doi.org/10.1016/j.tws.2008.04.005>

- Nie J, Fan J, Liu X, Huang Y (2013a) Comparative Study on Steel Plate Shear Walls Used in a High-Rise Building. *J Struct Eng*. [https://doi.org/10.1061/\(ASCE\)ST.1943-541X.0000613](https://doi.org/10.1061/(ASCE)ST.1943-541X.0000613)
- Nie J, Qin K, Cai CS (2008) Seismic behavior of connections composed of CFSSTCs and steel-concrete composite beams-experimental study. *J Constr Steel Res*. <https://doi.org/10.1016/j.jcsr.2007.12.004>
- Nie JG, Zhu L, Tao MX, Tang L (2013b) Shear strength of trapezoidal corrugated steel webs. *J Constr Steel Res*. <https://doi.org/10.1016/j.jcsr.2013.02.012>
- Park H-G, Kwack J-H, Jeon S-W, et al (2007) Framed Steel Plate Wall Behavior under Cyclic Lateral Loading. *J Struct Eng*. [https://doi.org/10.1061/\(ASCE\)0733-9445\(2007\)133:3\(378\)](https://doi.org/10.1061/(ASCE)0733-9445(2007)133:3(378))
- Paslar N, Farzampour A, Hatami F (2020) Infill plate interconnection effects on the structural behavior of steel plate shear walls. *Thin-Walled Struct*. <https://doi.org/10.1016/j.tws.2020.106621>
- Rafiei S, Hossain KMA, Lachemi M, Behdinan K (2015) Profiled sandwich composite wall with high-performance concrete subjected to monotonic shear. *J Constr Steel Res*. <https://doi.org/10.1016/j.jcsr.2015.01.015>
- Ryu HW, Kim HT, Kim YJ, Kim JW (2018) Determination of Combined Hardening Parameters to Simulate Deformation Behavior of C(T) Specimen under Cyclic Loading. In: *Procedia Structural Integrity*
- Sabelli R, Bruneau M (2006) *Steel Plate Shear Walls (Steel Design Guide 20)*. Am Inst Steel Constr Inc
- Shahmohammadi A, Mirghaderi R, Hajsadeghi M, Khanmohammadi M (2013) Application of corrugated plates as the web of steel coupling beams. *J Constr Steel Res*. <https://doi.org/10.1016/j.jcsr.2013.02.009>
- Shi Y, Wang M, Wang Y (2011) Experimental and constitutive model study of structural steel under cyclic loading. *J Constr Steel Res*. <https://doi.org/10.1016/j.jcsr.2011.02.011>
- Shon S, Yoo M, Lee S (2017) An experimental study on the shear hysteresis and energy dissipation of the steel frame with a trapezoidal-corrugated steel plate. *Materials (Basel)*. <https://doi.org/10.3390/ma10030261>
- Tessler A, Spiridigliozzi L (1988) Resolving membrane and shear locking phenomena in curved shear-deformable axisymmetric shell elements. *Int J Numer Methods Eng*. <https://doi.org/10.1002/nme.1620260506>
- Thorburn LJ, Kulak GL, Montgomery CJ (1983) Analysis of steel plate shear walls. *Struct Eng Report 107*, Dep Civ Eng Univ Alberta, Alberta, Canada
- Vian D, Bruneau M, Tsai KC, Lin Y-C (2009) Special Perforated Steel Plate Shear Walls with Reduced Beam Section Anchor Beams. I: Experimental Investigation. *J Struct Eng*. [https://doi.org/10.1061/\(ASCE\)0733-9445\(2009\)135:3\(221\)](https://doi.org/10.1061/(ASCE)0733-9445(2009)135:3(221))

- Vigh LG, Liel AB, Deierlein GG, et al (2014) Component model calibration for cyclic behavior of a corrugated shear wall. *Thin-Walled Struct.* <https://doi.org/10.1016/j.tws.2013.10.011>
- Wang M, Yang W, Shi Y, Xu J (2015) Seismic behaviors of steel plate shear wall structures with construction details and materials. *J Constr Steel Res.* <https://doi.org/10.1016/j.jcsr.2015.01.007>
- Ye Z, Berdichevsky VL, Yu W (2014) An equivalent classical plate model of corrugated structures. *Int J Solids Struct.* <https://doi.org/10.1016/j.ijsolstr.2014.02.025>
- Yi J, Gil H, Youm K, Lee H (2008) Interactive shear buckling behavior of trapezoidally corrugated steel webs. *Eng Struct.* <https://doi.org/10.1016/j.engstruct.2007.11.009>
- Youssef N, Wilkerson R, Fischer K, Tunick D (2010) Seismic performance of a 55-story steel plate shear wall. *Struct Des Tall Spec Build.* <https://doi.org/10.1002/tal.545>
- Yousuf M, Bagchi A (2010) Seismic performance of a 20-story steel-frame building in Canada. *Struct Des Tall Spec Build.* <https://doi.org/10.1002/tal.517>
- Zhao Q, Sun J, Li Y, Li Z (2017) Cyclic analyses of corrugated steel plate shear walls. In: *Structural Design of Tall and Special Buildings*

Tables

Table 1 Parametric Case Study

Group #	Notation	Wall type	Thickness (mm)	Welding separation		Parameter
				Location	Length (mm)	
S*	SPt6.75	Plane	6.75	N/A	N/A	Infill type
	SPt5	Plane	5	N/A	N/A	
	SHt5	H-Corrugated		N/A	N/A	
	SVt5	V-Corrugated		N/A	N/A	
	SPt5-HS	Plane		N/A	N/A	
	PS1	Plane		Column	3000	
PS2	Plane		Beam	3000		
PS3	Plane		Beam	1000		
PS4	Plane		Beam	1000		
PS5	Plane		Beam	2000		
W**	WHt5	H-Corrugated		N/A	N/A	Boundary Stiffness
	WVt5	V-Corrugated		N/A	N/A	
	WPt5	Plane		N/A	N/A	
	WPt5-HS	Plane		N/A	N/A	

* Strong boundary frame with HW400*400*13*21 for Columns and HM 500*300*11*15 for beams.

**Weak boundary frame HW 350*350*12*19 for Column and HM 400*300*10*16 for beams.

Table 2 Hardening Parameters of Materials (ABAQUS)

Parameter	Value, N/mm ²	Parameter	Value
Q_{∞}	21	b	1.2
C_1	7993	γ_1	175
C_2	6773	γ_2	116
C_3	2854	γ_3	34
C_4	1450	γ_4	29

Where, C is the kinematic hardening modulus, γ is the rate at which hardening modulus decreases with the plastic strain, Q_{∞} is the maximum change in the size of the yield surface,

and b is the rate at which initial yield stress change with the plastic strain.

Table 3 Cyclic Results of SPSWS, Stiffened SPSW and COSPSW

Model	Direction	K_1 (kN/mm)	K_2 (kN/mm)	Δ_y (mm)	V_y (kN)	Δ_m (mm)	V_m (kN)
SPt5	push -	300.8	152.13	16.3	2479.5	130	3267.17
	pull +	299.9	158.1	16.3	2855.2	130	3203.4
SPt6.75	push -	369.7	186.88	16.3	2433	130	3511.95
	pull +	369.25	196.16	16.3	3521.3	130	3507.93
SHt5	push -	275.49	174.4	16.3	2823.95	32.5	2984.27
	pull +	275.492	175.57	16.3	2823	32.5	3225.2
SVt5	push -	271.83	175.85	8.1	2208.7	32.5	3042.45
	pull +	271.93	173.8	16.3	2812.1	32.5	3093.0
SPt5-HS	push -	303.17	166.18	8.1	2472.1	130	4016.8
	pull +	302	162.6	8.1	2463.2	130	3989.5

Where K_i is the initial stiffness, K_2 is the second cyclic stiffness, Δ_y represents yield displacement, V_y represents yield force, Δ_m represents displacement at maximum lateral capacity, and V_m represents maximum lateral strength capacity.

Table 4 Cyclic Results of SPSWS, COSPSW and Stiffened SPSW with Weak Frame

Model	Direction	K_1 (kN/mm)	K_2 (kN/mm)	Δ_y (mm)	V_y (kN)	Δ_m (mm)	V_m (kN)
SPt5	push -	300.8	152.1	16.3	2479.5	130	3267.1
	pull +	299.9	158.08	16.3	2855.2	130	3203.3
WPt5	push -	287.05	127.5	8.1	2326.8	130	2673.05
	pull +	286.30	126.3	8.1	2332.2	130	2686.04
SHt5	push -	275.49	174.4	16.3	2823.95	32.5	2984.27
	pull +	275.49	175.57	16.3	2823	32.5	3225.2
WHt5	push -	258.34	161.697	8.1	2099	16.25	2627.59
	pull +	258.36	163	16.3	2626.4	32.5	2788.6
SVt5	push -	271.83	175.85	8.1	2208.7	32.5	3042.45
	pull +	271.93	173.8	16.3	2812.1	32.5	3093.04
WVt5	push -	256.09	163.8	16.3	2648.8	32.5	2697.0
	pull +	256.19	162.5	16.3	2625.6	32.5	2735.0
SPt5-HS	push -	303.1	166.18	8.1	2472.1	130	4016.79
	pull +	302	162.6	8.1	2463.2	130	3989.5
WPt5-HS	push -	289.29	152.7	16.3	2480	130	3383.4
	pull +	288.2	157.0	16.3	2701	130	3429.17

Where K_1 is the initial stiffness, K_2 is the second cyclic stiffness, Δ_y represents yield displacement, V_y represents yield force, Δ_m represents displacement at maximum lateral capacity, and V_m represents maximum lateral strength capacity.

Table 5 Cyclic Results of Steel Walls with Different Welding Separation Characteristics.

Model	Load direction	K_1 (kN/mm)	K_2 (kN/mm)	Δ_y (mm)	V_y (kN)	Δ_m (mm)	V_m (kN)
SPt5	push -	300.77	152.12	16	2479.5	130	3267.17
	pull +	299.91	158.1	16	2855.2	130	3203.4
PS1	push -	238.9	107.4	8.12	1958.2	130	2852.6
	pull +	235.4	110.6	8.12	1939	130	2868.6
PS2	push -	193.47	105.85	8.12	2000.5	130	2759.1
	pull +	245.17	106	8.12	2016.8	130	2757.5
PS3	push -	239.81	143.6	8.12	2384.2	130	3173.23
	pull +	244.61	136.05	8.12	2367.9	130	3169.91
PS4	push -	235.4	141.13	8.12	2333.7	130	3272.5
	pull +	245.9	139.25	8.12	2310.15	130	3207.81
PS5	push -	271.0	129.45	16.3	2143.6	130	3144.28
	pull +	268.65	130.34	8.12	2204.1	130	2860.98

Where K_i is the initial stiffness, K_2 is the second cyclic stiffness, Δ_y represents yield displacement, V_y represents yield force, Δ_m represents displacement at maximum lateral capacity, and V_m represents maximum lateral strength capacity.

Figures

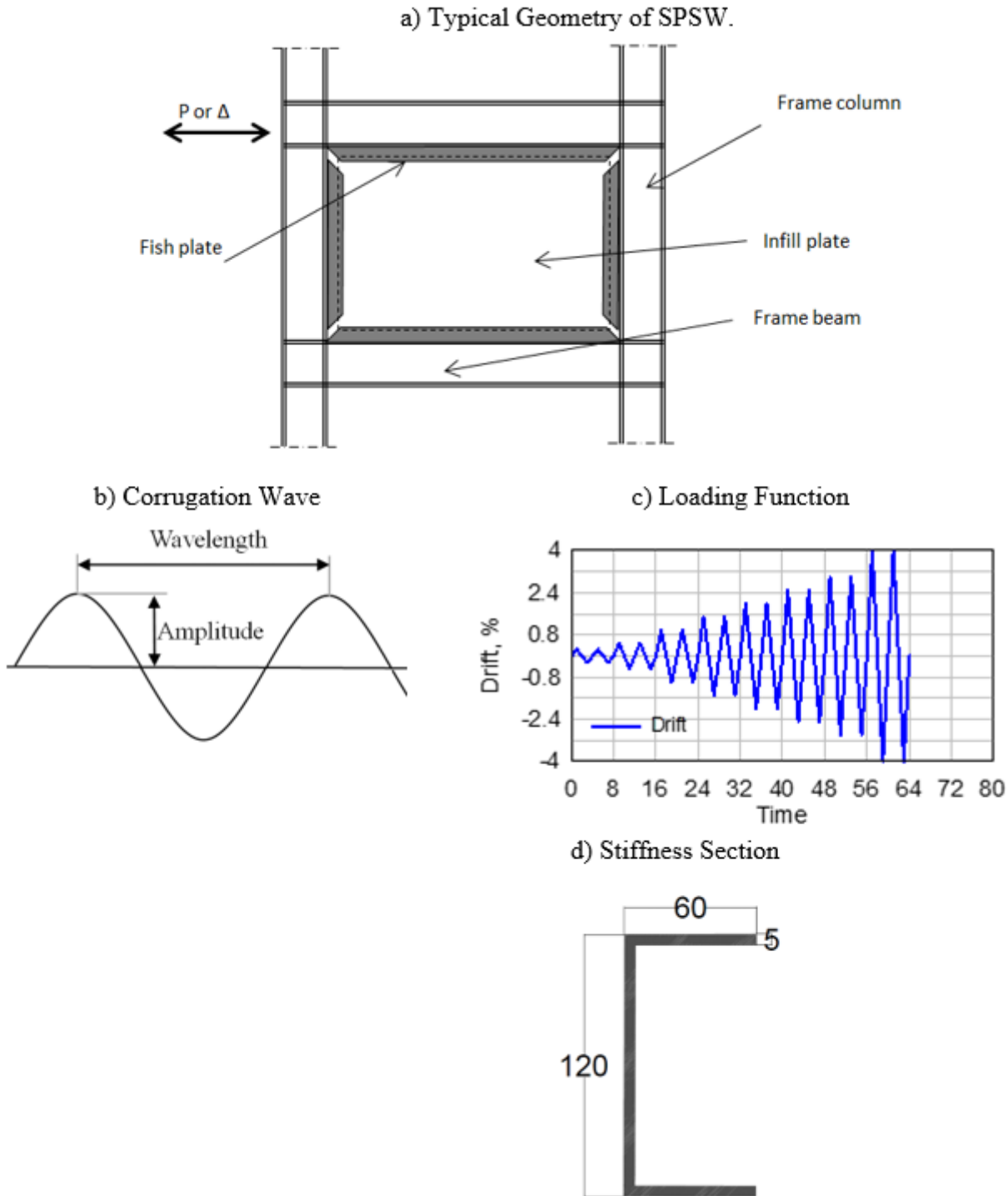


Figure 1

Corrugated Sheet Shear Walls: a) Main elements, b) Corrugated sheet geometry, c) Loading function, and d) Stiffness cross-section.

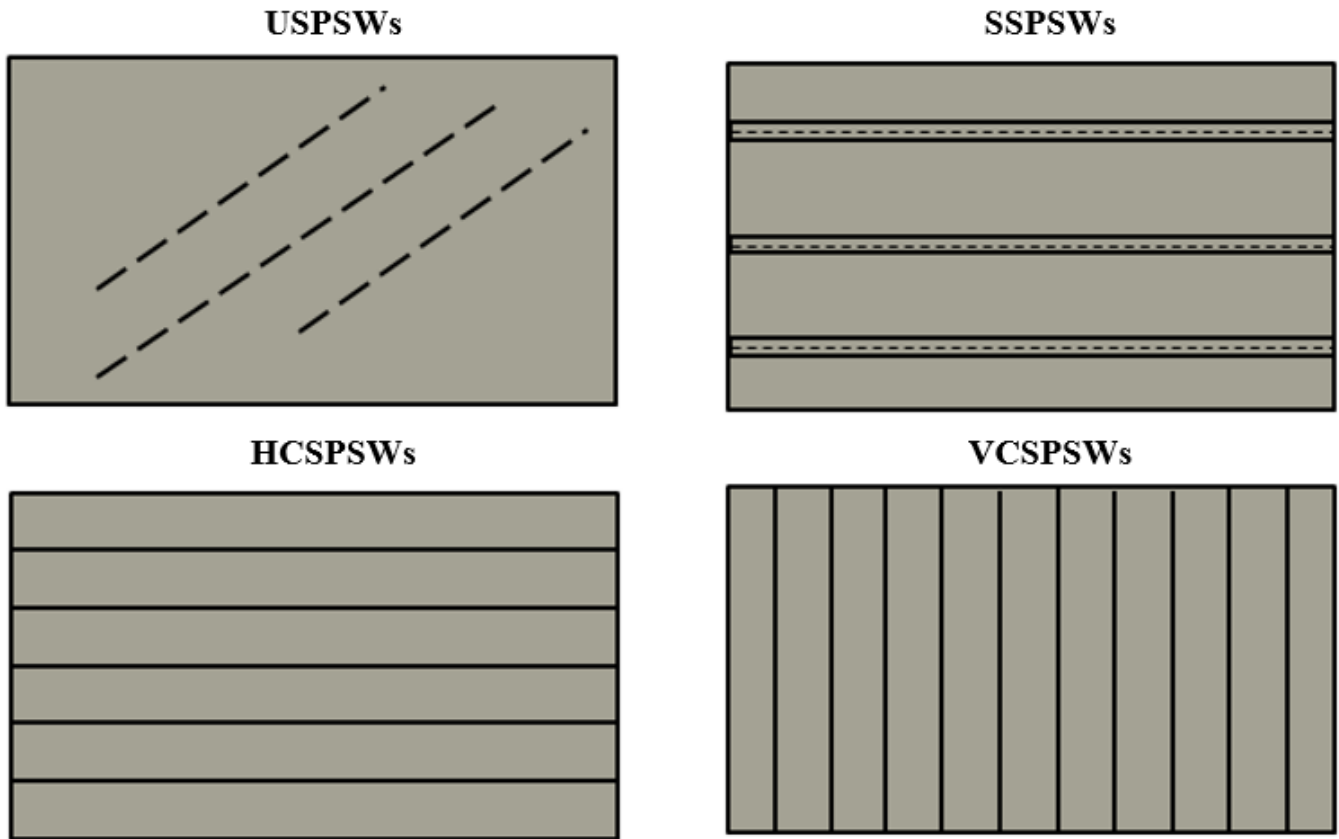


Figure 2

Geometry of different SPSWs types USPSWs, SSPSWs, HCSPSWs, and VCSPSWs.

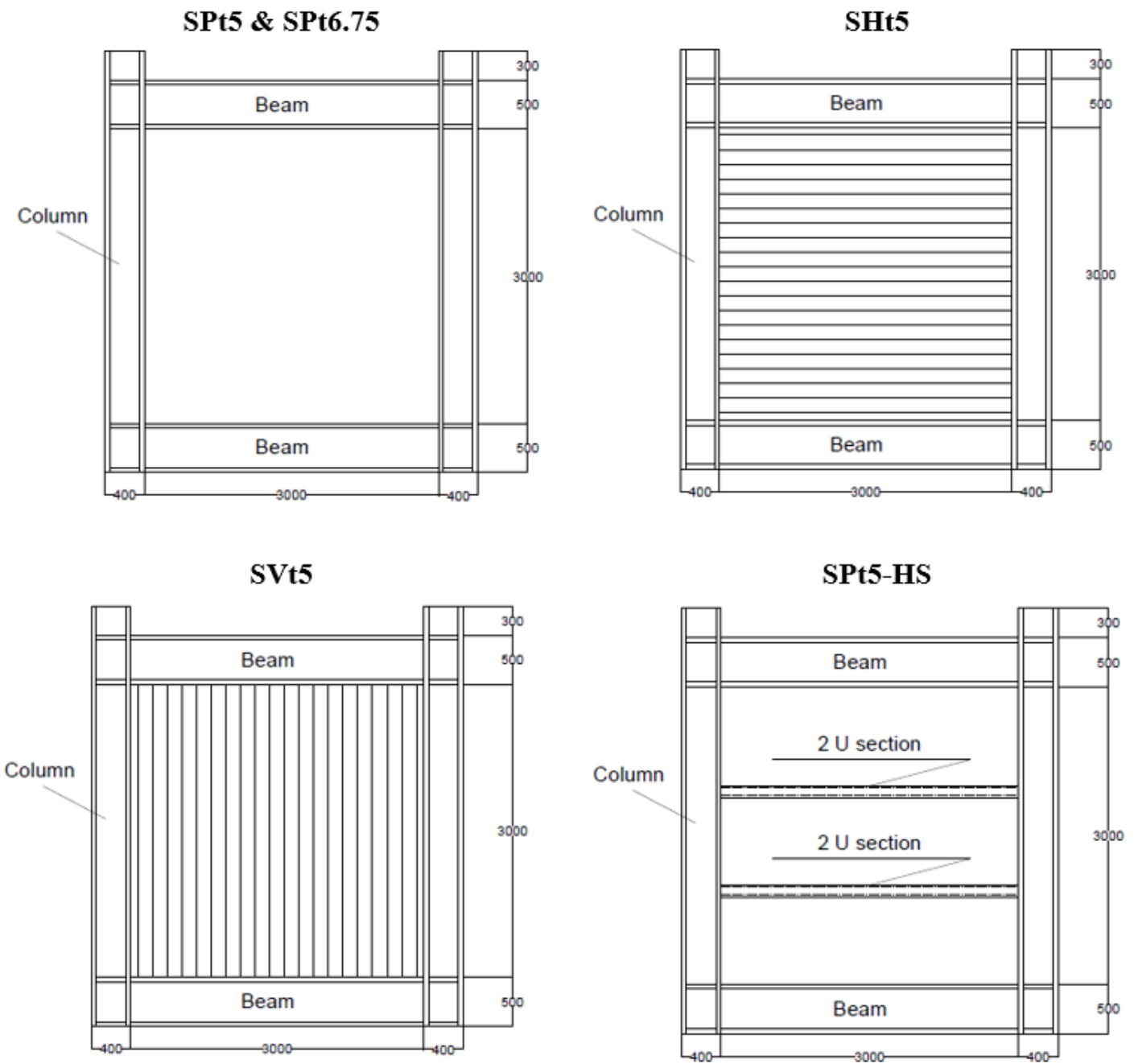


Figure 3

Geometry of strong case SPt5 & SPt6.75, SHt5, SVt5, and SPt5-HS.

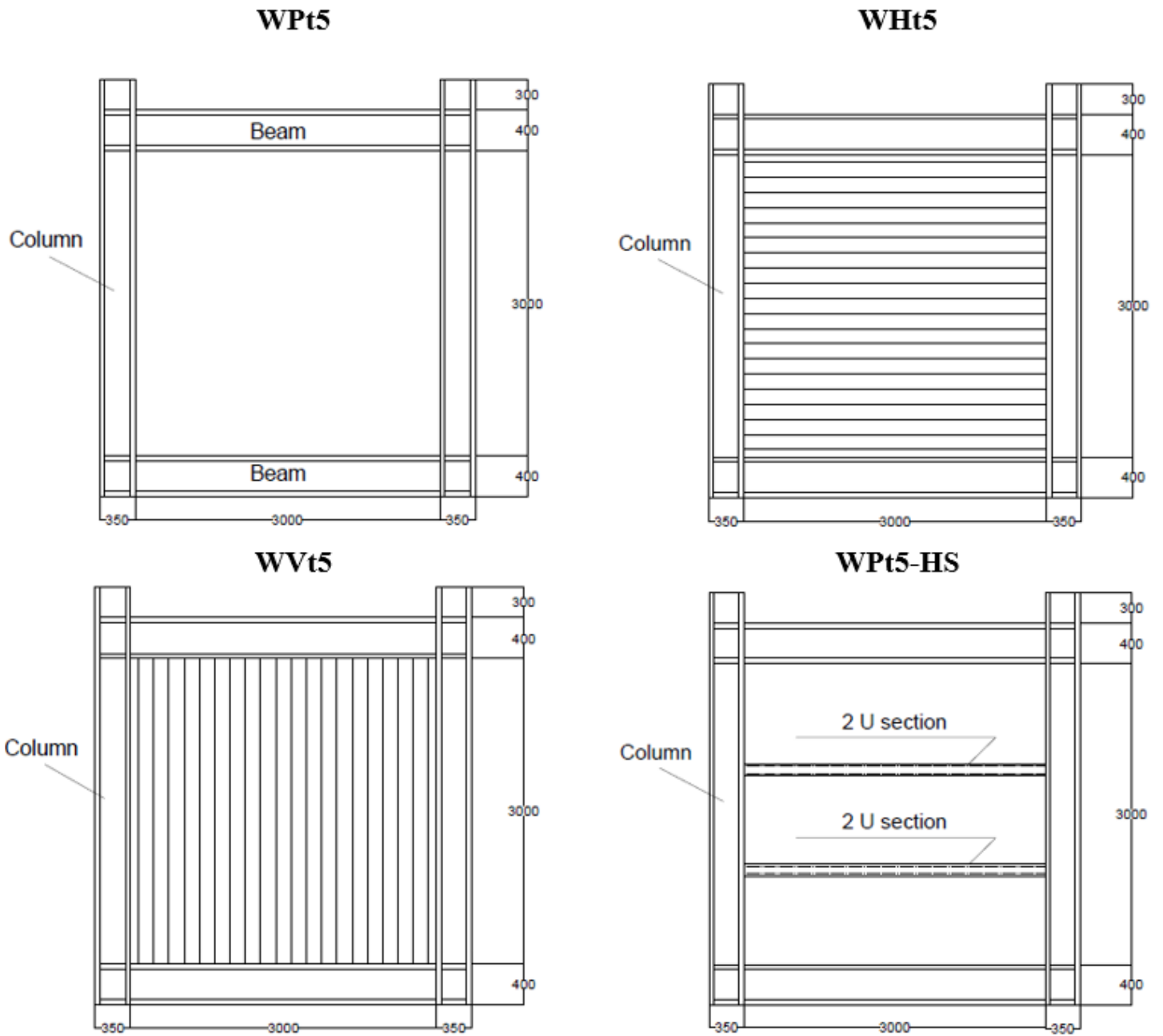


Figure 4

Geometry of weak case WPt5, WHt5, WVt5, and WPt5-HS.

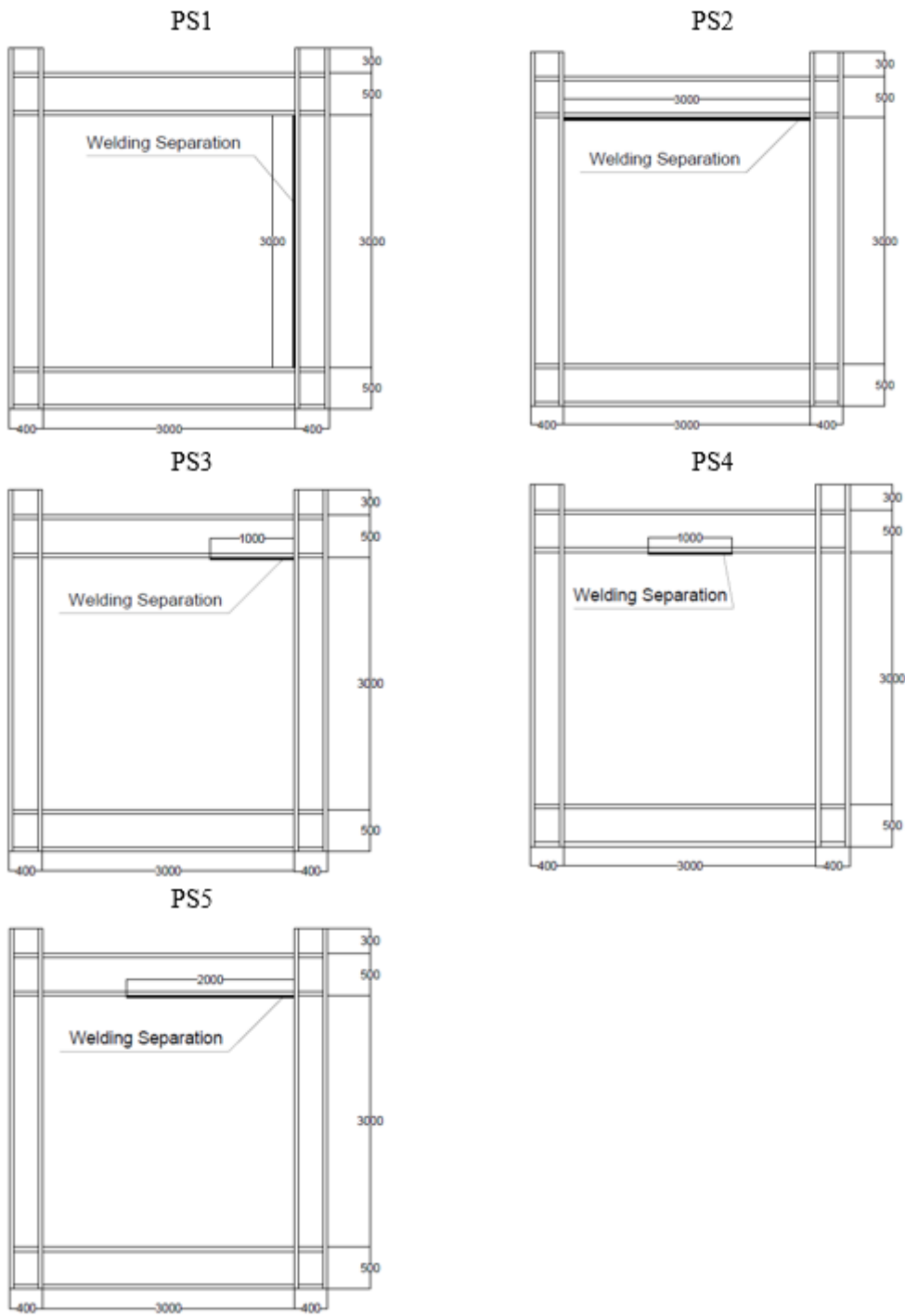
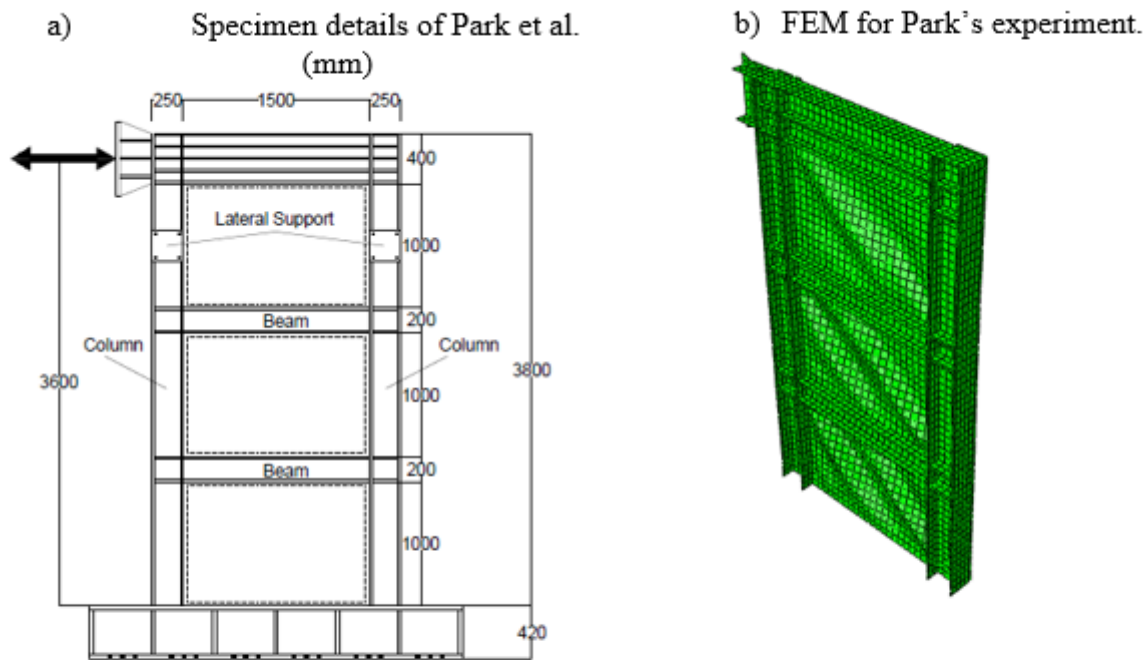


Figure 5

Details of Plate Welding Separation Characteristics with Boundary Frame (Dimensions in mm).



c) Comparisons between experimental and numerical results.

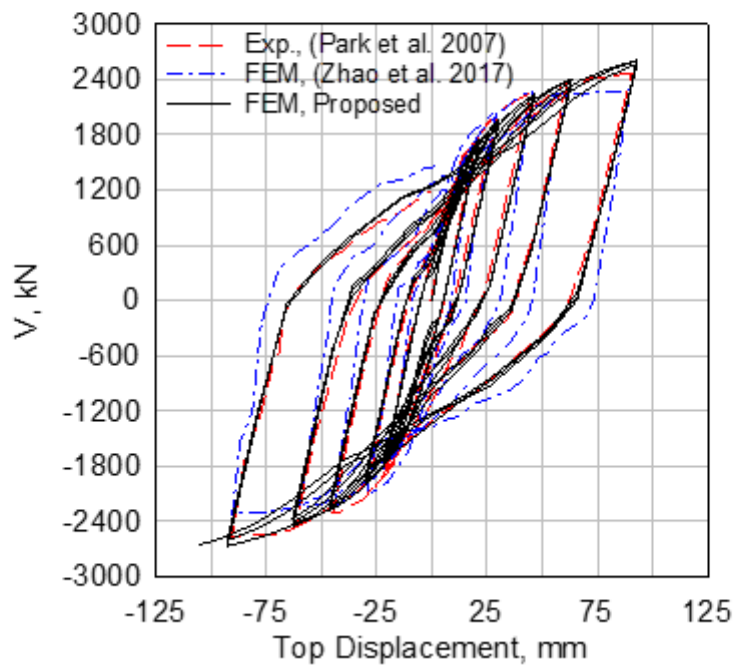
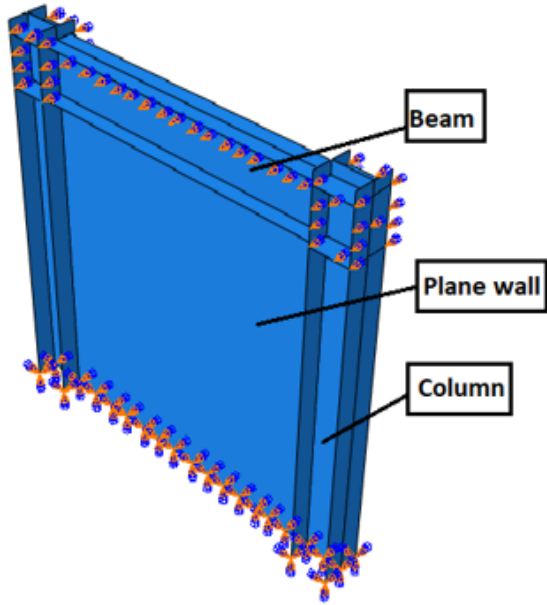


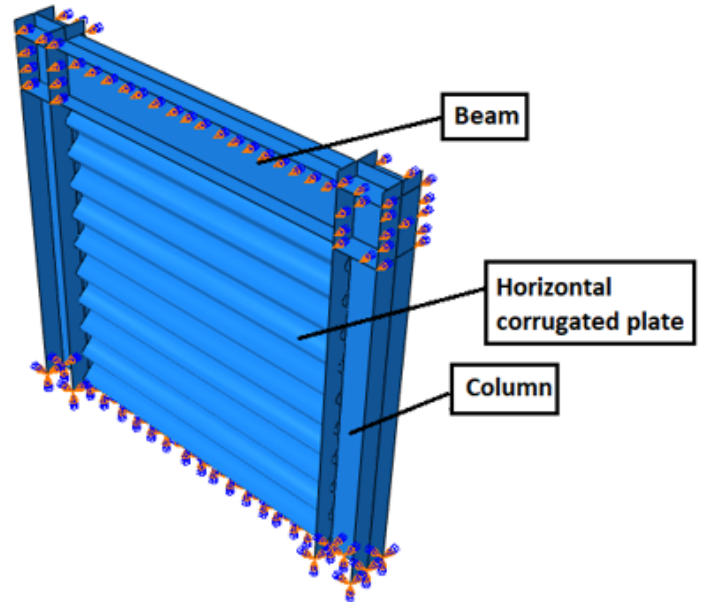
Figure 6

Finite Element Experimental Validation; a) Specimen details (mm), b) Finite element model deformed shape, and c) Comparison between proposed FEM and experimental results.

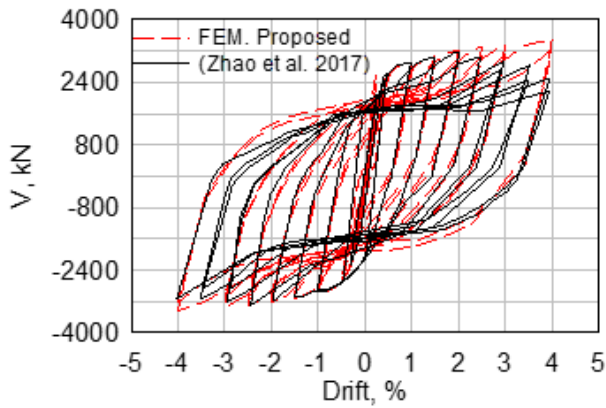
a) FEM of SC-PW for Zhao et al. 2017



b) FEM of SC-HSW for Zhao et al. 2017



c) SC-PW results comparison



d) SC-HSW results comparison

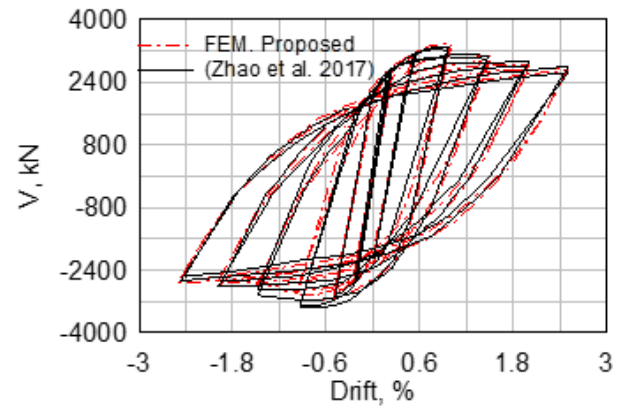
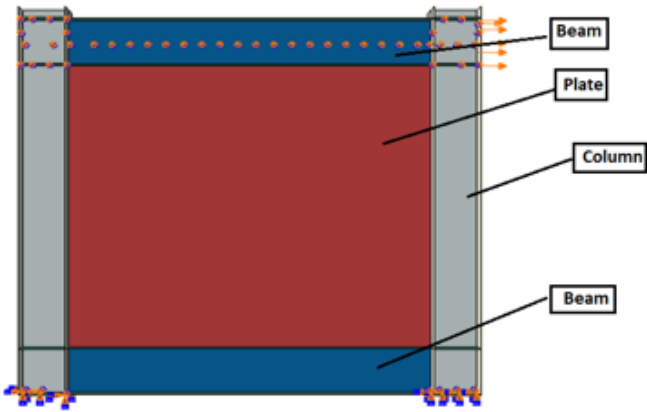
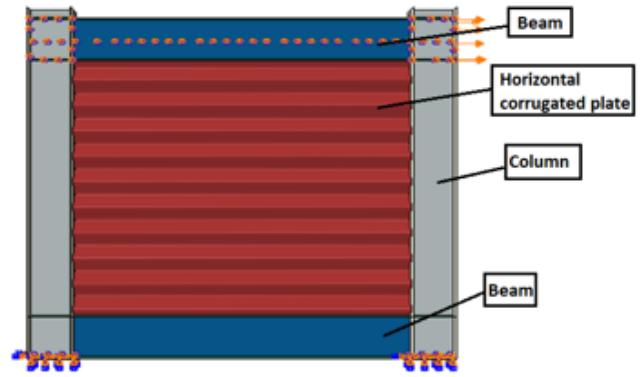


Figure 7

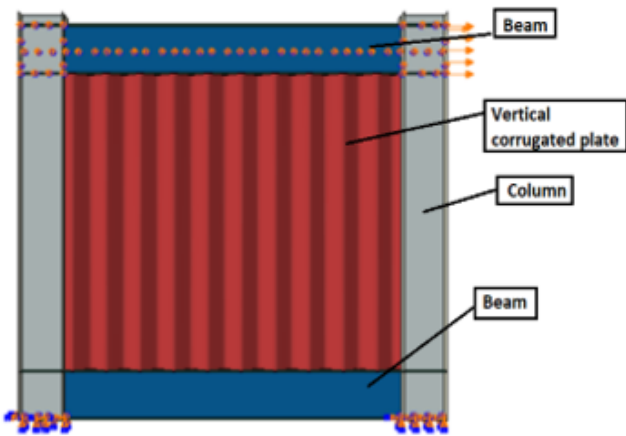
Finite Element Numerical Validation; a) FEM of SC-PW, b) FEM of SC-HSW, c), and d) Comparison between Zhao et al. 2017 results and proposed FEM for SC-PW and SC-HSW.



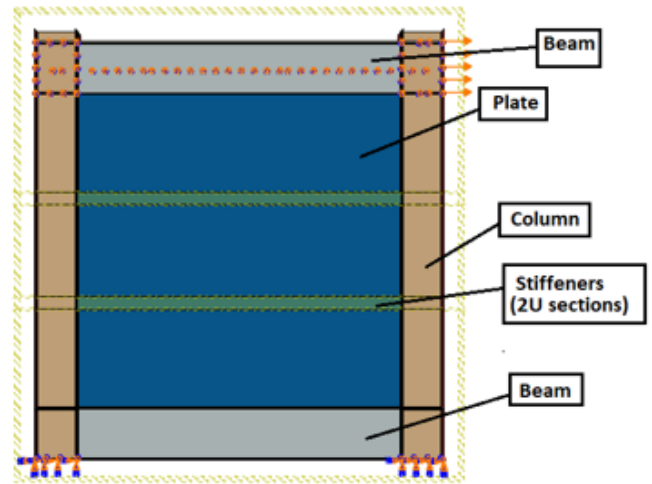
a) SPt5 & SPt6.75



b) SHt5



c) SVt5



d) SPt5-HS

Figure 8

Geometry of the Finite Element Models for Strong Case.

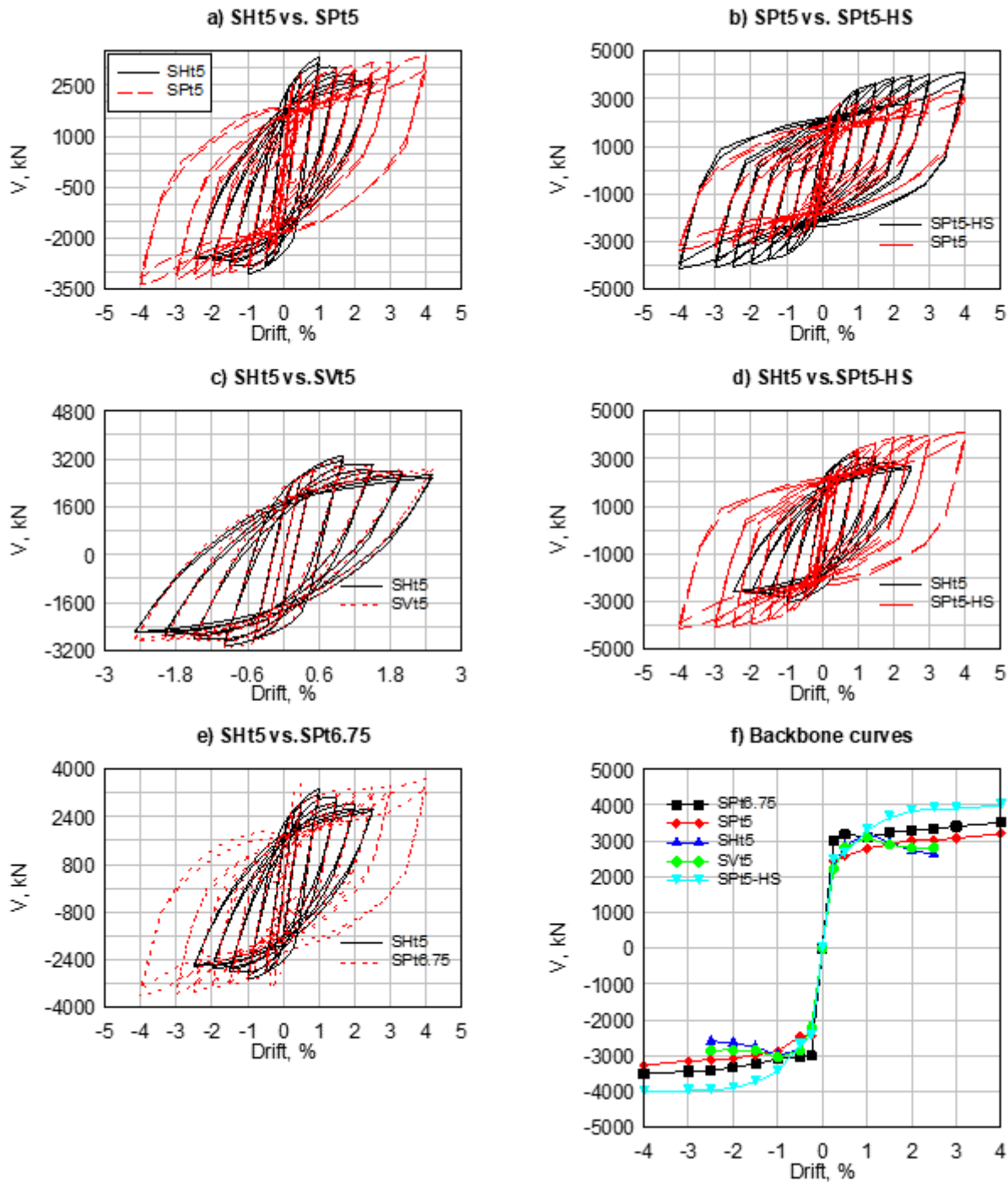


Figure 9

Comparison between Different Hysteretic and Backbone Curves of USPSW, CSPSW, and SSPSW with Strong Case.

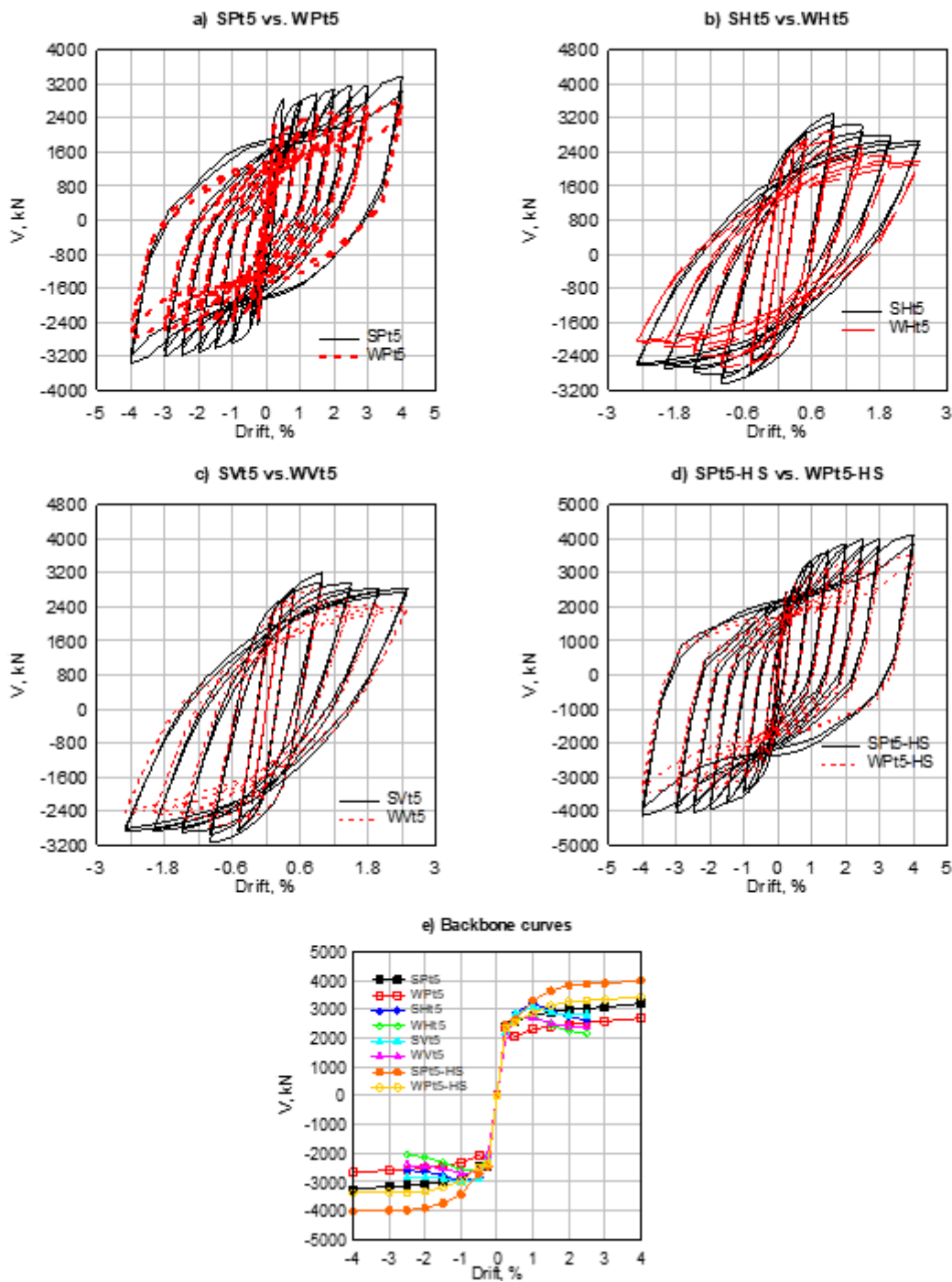


Figure 10

Comparison between Different Hysteretic and Backbone Curves of USPSW, CSPSW, and SSPSW with Different Boundary Frames.

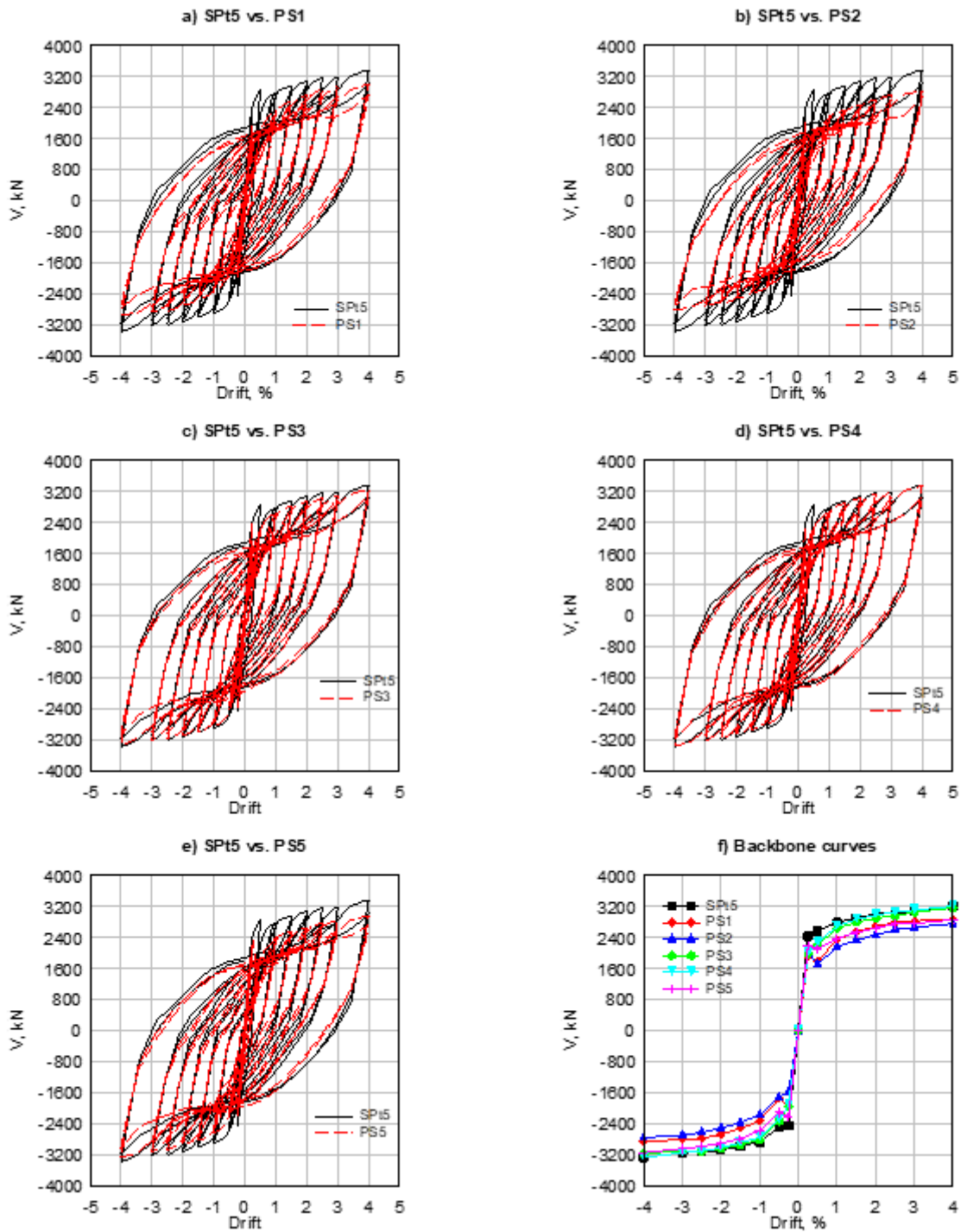


Figure 11

Comparisons between Hysteretic and Backbone Curves of USPSW with Different Welding Separation.

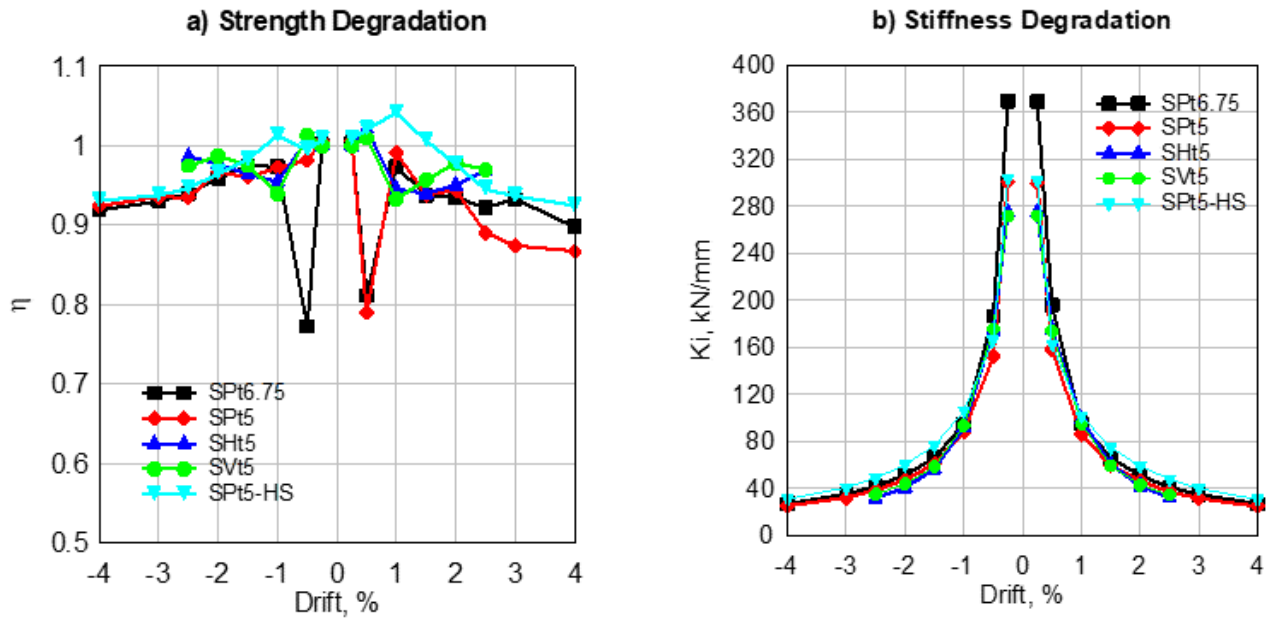


Figure 12

Degradation Characteristics of USPSW, SSPSW, and CSPSW with Strong Case; a) Strength degradation, and b) Stiffness degradation.

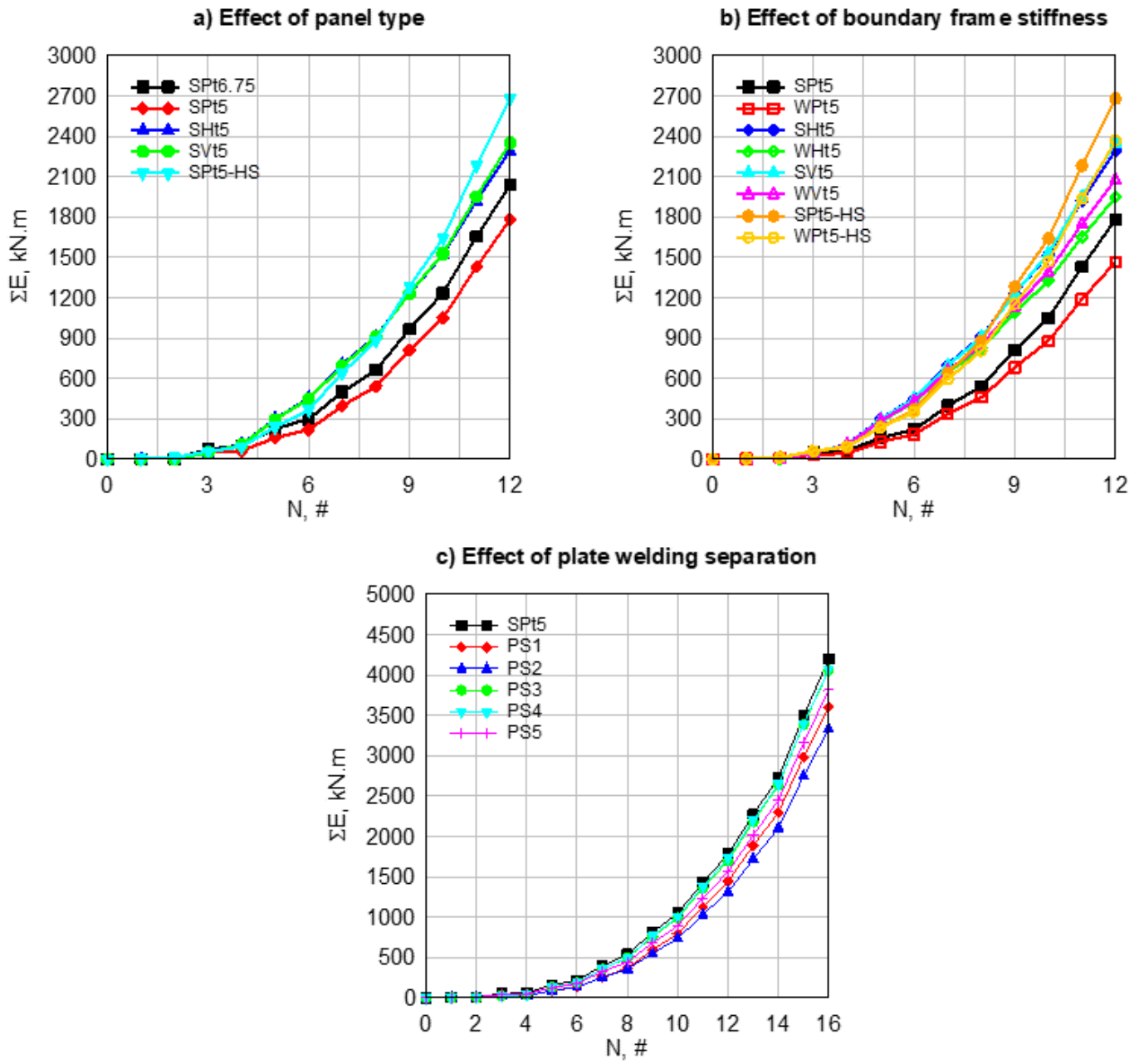


Figure 13

Accumulated Energy Dissipation Capacity of USPSW, SSPSW, and CSPSW.

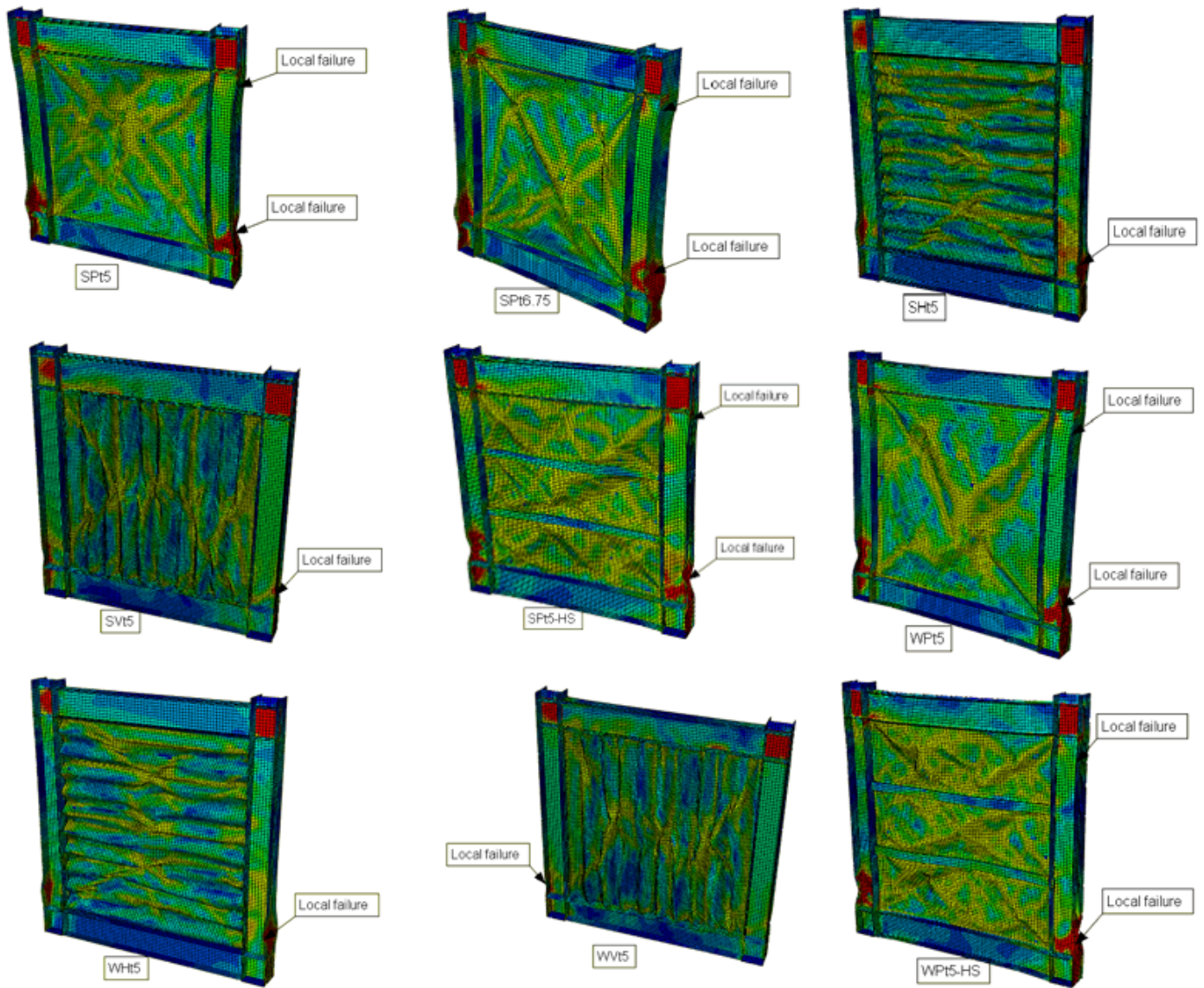


Figure 14

Comparison between Systems Failure Modes of Strong and Weak Cases.

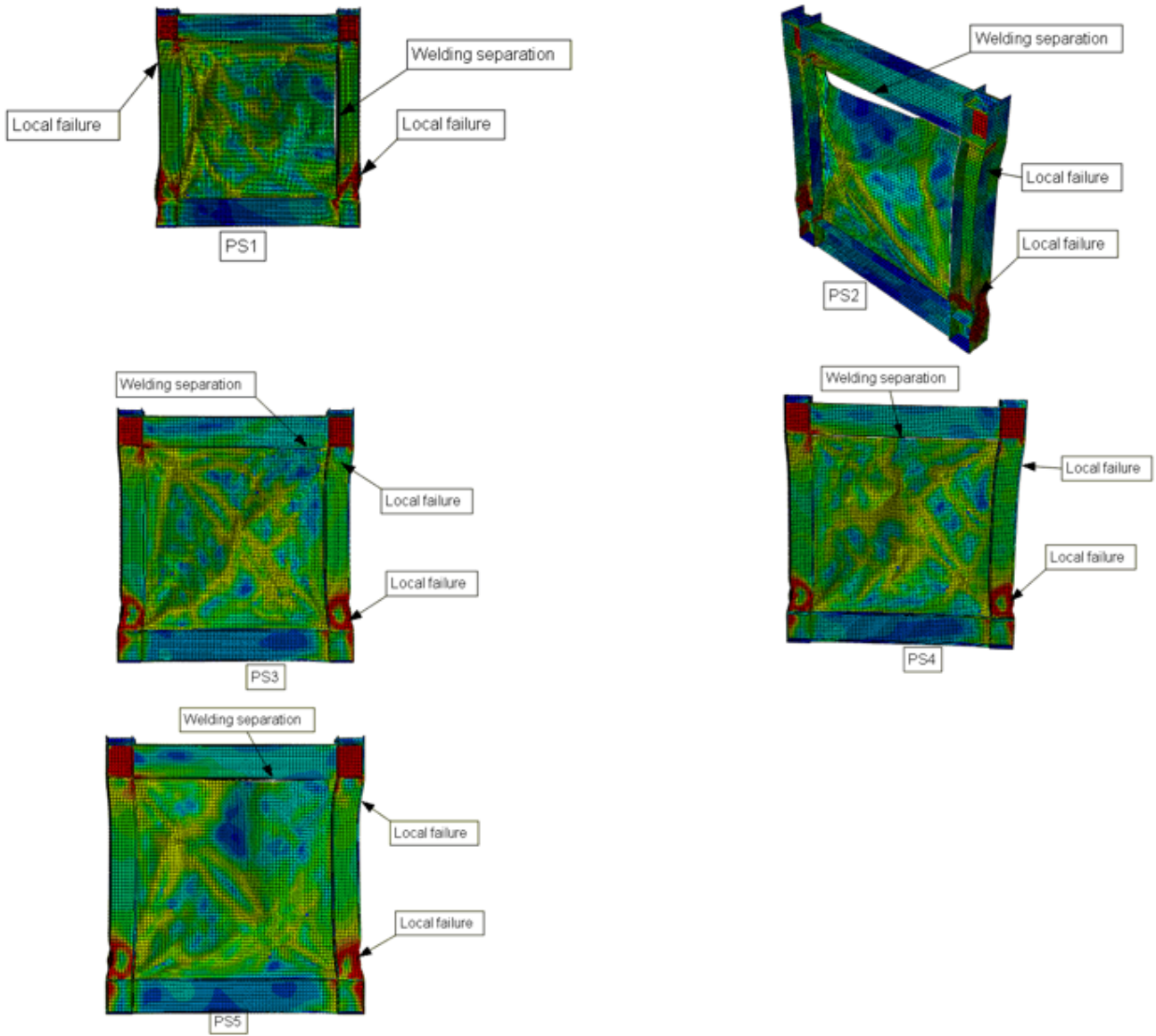


Figure 15

Comparison between Systems Failure Modes with Welding Separation.